



Cite this: *Dalton Trans.*, 2025, **54**, 14618

## Design and transformation of ACQphores into AIEgens: toward MOF-based advanced sensing applications

Khushboo Rathore,<sup>a</sup> Anita Nehra  <sup>\*b,c</sup> and Ritambhara Jangir  <sup>\*a</sup>

Aggregation-induced emission (AIE) has emerged as a groundbreaking optoelectronic phenomenon that overcomes the limitations of aggregation-caused quenching (ACQ), enabling the development of highly light-emitting substances with broad applications. This overview presents a detailed exploration of AIE and ACQ, discussing their historical background, fundamental definitions, and working mechanisms, particularly the restriction of intramolecular rotations (RIRs), vibrations (RIVs), and motions (RIMs). Significant focus is placed on the transformation strategies for converting ACQ-active fluorophores (ACQphores) into AIE-active luminogens (AIEgens). Beyond molecular design, this review delves into the rapidly expanding field of AIE-based metal–organic frameworks (AIE-MOFs) and their utilization in sensing. Various AIE-MOF systems developed for the sensing of biological molecules, volatile organic compounds (VOCs), heterocyclic compounds, and nitroaromatic explosives are discussed, demonstrating their exceptional sensitivity, selectivity, and stability. Additionally, stimuli-responsive luminescent materials capable of detecting changes in temperature, pressure, and pH are discussed, showcasing their potential for dynamic environmental sensing. Overall, this review highlights the synergy between AIE and MOF chemistry, with a distinct emphasis on the mechanistic transformation of ACQphores into AIEgens and their structural influence on emissive behaviour. Unlike broader reviews, this article is specifically organized around the sensing applications of AIE-MOFs, classifying them by analyte type and thereby exploring multifunctional AIE-MOF platforms for advanced sensing and imaging applications.

Received 16th July 2025,  
Accepted 9th August 2025

DOI: 10.1039/d5dt01669j

rsc.li/dalton

### 1. Introduction

Light has always been, and remains, a crucial and essential component of life and society.<sup>1</sup> Advances in the comprehension and use of light-responsive or emitting materials have paved the way for new scientific and societal benefits. The study of luminescent/photoemissive (PE) materials, which emit light as a response to any stimuli, continues to be a key area of attention in the research fraternity owing to their immense potential in fields such as bioimaging, chemosensing, photoluminescence, therapeutics, and electroluminescence devices.<sup>2</sup> PE compounds can ideally exist in all physical states: gas, liquid, and solid. However, in most real-world applications, these luminophores, the moieties in a compound that are accountable for light emission, are primarily utilized in thin films and clustered states. For instance, in optoelectronic requirements such as OLEDs (organic light-emitting

diodes) and OFETs (organic field-effect transistors), luminophores are typically employed as thin solid films and crystals. Alternatively, in biomedical research, they are often used in physiological environments or water-based media. Furthermore, by adding polar functional groups to the molecular structures of luminophores, their solubility in water can be improved. An example is the synthesis of a series of water-soluble solvatochromic fluorophores through the introduction of oligoethylene glycol chains into their molecular structures.<sup>3</sup> However, the inherent hydrophobic nature of their aromatic constituents (such as phenyl or polyphenyl units) still leads to the assembly of nanoclusters that are too small to be seen with the naked eye. This issue also arises when organic fluorophores (compounds that emit light by relaxing from the singlet excited state) are used for tracking ecosystems and protecting the environment.

Traditional research on organic luminescence has predominantly been carried out in solution.<sup>4–8</sup> Photophysical properties, including luminescence efficacy, decomposition rate, and exciton lifetime, are generally evaluated or quantified in extremely dilute mixtures. These solution-based investigations have significantly advanced the core comprehension of light-emission mechanisms at the molecular scale. However, the

<sup>a</sup>Department of Chemistry, Sardar Vallabhbhai National Institute of Technology (SVNIT), Surat-395007, Gujarat, India. E-mail: ritambhara.jangir@chem.svnit.ac.in

<sup>b</sup>The LNM Institute of Information Technology, Jaipur-302031, Rajasthan, India

<sup>c</sup>Department of Chemistry, JECRC University, Sitapura Extension, Jaipur-303905, India

deductions derived from data obtained in dilute solutions are not generally applicable to concentrated solutions. In fact, numerous organic fluorophores exhibit markedly varying photoluminescent characteristics with a variation in their concentration. Generally, their luminescence is reduced at elevated molarities due to the formation of aggregates.<sup>9,10</sup> Thus, the phenomenon of partial or total suppression of luminescence resulting from cluster formation/aggregates is referred to as aggregation-caused quenching (ACQ). This effect is primarily ascribed to a dense arrangement of light-emitting molecules that possess significant planar  $\pi$ -segments.<sup>11</sup> In contrast, some molecules exhibiting luminescence in the aggregated state received significantly less attention earlier. In 2001, Ben Zhong Tang introduced this phenomenon as aggregation-induced emission (AIE). This is shown by luminophores that exhibit little to no luminescence in dilute medium but are strongly luminescent when arranged closely in a concentrated solution.<sup>12</sup> This advancement has transformed the molecular design of light-emitting substances.<sup>9,13–21</sup> Further, the research works on AIE led to the development of light-emitting materials in the solid-state, which have real-world implications, consequently advancing to previously unthinkable technological breakthroughs.<sup>17,22–27</sup> These luminogens that exhibit AIE attributes are called AIEgens, which is an analog term for “mesogens” used for molecules that exhibit mesomorphism under appropriate conditions, such as at elevated temperatures, in the realm of liquid crystals. Many attempts have been made to investigate the fundamental mechanism of AIE.<sup>9,13–15</sup> A number of tenable hypotheses have been put forth, such as excited-state intramolecular proton transfer, conformational planarization, the creation of J-aggregates or excimers, and restriction of intramolecular motion (RIM). RIM includes restriction of intramolecular vibrations (RIV) and restriction of intramolecular rotations (RIR), which explains AIE mechanism more thoroughly. According to this, in diluted solutions with few interactions between the AIEgen molecules, the excited energy is used by AIEgens in non-luminous emissive processes such as free vibration, rotation, and motion. These nonradiative routes are blocked in the aggregates by RIM due to conformational stiffening, thereby showing either phosphorescence or fluorescence.<sup>11</sup>

Conversely, the study of ACQ has a much longer history than AIE;<sup>28</sup> thus, its operational process has been thoroughly comprehended.<sup>10</sup> However, although luminophores with ACQ, known as ACQphores, have been used in wide range of practical applications, fully harnessing their potential in solid form has been challenging. Typically, the performance of a luminophore in the solid state is not as good as in solution, and if its emission in solution is inefficient, the chances of finding viable applications for its solid form are slim. However, AIEgens challenge this conventional view, demonstrating that materials previously considered ineffective can actually be extremely versatile. Emission properties that were tough to achieve with traditional ACQphores can now be easily accomplished with AIEgens.<sup>14</sup>

AIE has created novel opportunities for a wide range of possibilities, offering significant potential for advanced techno-

logical innovations.<sup>9,13,15–20,29</sup> AIEgens have proven effective as fluorescence “turn-on” or “light-up” bioanalytical devices,<sup>16,17,30</sup> and as probes for biological processes.<sup>31</sup> Moreover, highly luminescent nano-objects, such as AIE dots, are currently making a significant impact in the field of bioimaging,<sup>15,16,21</sup> such as targeted imaging of organelles,<sup>15,32–34</sup> tissues,<sup>15,35</sup> cells,<sup>15,16</sup> and microbes.<sup>36</sup> Various AIE-based chemosensing platforms have been investigated for a broad spectrum of target molecules, including explosives,<sup>37</sup> ions,<sup>38,39</sup> organic small molecules<sup>40</sup> and fingerprints.<sup>41</sup> The identification of these factors is crucial for safeguarding the environment, monitoring water quality, ensuring national safety, and conducting criminological investigations. Recent studies have significantly advanced the understanding of light-induced emission phenomena by dissecting the mechanistic basis of AIE and ACQ. These works collectively emphasize how molecular conformation and packing status, electronic transitions, and environmental interactions (such as intermolecular hydrogen bonding and  $\pi$ - $\pi$  stacking) govern radiative and nonradiative pathways, thereby modulating the fluorescence efficiency across the solution and solid states.<sup>42–46</sup> AIEgens have been integrated in diverse opto-electronic frameworks by leveraging their benefits as highly effective solid-state emission systems in circularly polarized luminescence (CPL) systems,<sup>47</sup> OLED devices,<sup>15</sup> liquid crystal displays,<sup>48</sup> and optical waveguides.<sup>33</sup> AIEgens can be affected by external factors, including mechanical pressure, changes in temperature, fluctuations in pH, exposure to harmful vapors, and light irradiation. Several stimuli-responsive AIE-active smart materials have been developed that incorporate a combination of thermos,<sup>49</sup> photochromisms,<sup>50</sup> mechano,<sup>18</sup> and vapo<sup>51</sup> properties.

Metal-organic frameworks (MOFs) are composite materials that combine organic and inorganic components, featuring a variety of structures, extensive surface areas, and multifunctional capabilities. They represent the first group of highly ordered crystalline porous materials created through reticular chemistry. MOFs are constructed by integrating clusters or metal ions with organic bridging units. In recent years, hybrid materials have been developed successfully by combining MOFs with various functional components, such as metal oxides,<sup>52</sup> ionic liquids,<sup>53,54</sup> polymers,<sup>55</sup> nanoparticles,<sup>56,57</sup> carbonaceous materials,<sup>58</sup> biomolecules,<sup>59</sup> perovskites,<sup>60</sup> and other MOFs,<sup>61</sup> enabling them to retain the characteristics of each constituent, while exhibiting novel synergistic properties. Due to the wide range of available metal ion types, organic binding units, and complexation arrangements, various MOFs have been developed, demonstrating significant potential in utilities such as drug delivery, gas storage and separation, catalysis, energy storage, sensing, controlled release systems, multimodal tracers, and flame-retardant materials.<sup>62–77</sup> Lately, researchers have shown substantial interest in using AIEgens to create luminescent MOFs.<sup>37,78–89</sup> In contrast to small molecular AIEgens, which interact unpredictably through non-covalent bonds when aggregated, the AIE building units in MOFs are securely positioned in predetermined locations

through covalent or coordinate bonds, supported by non-covalent interactions within the framework. Considerable research efforts have been dedicated to developing luminescent MOFs, owing to their easily modifiable surfaces and adjustable porosity, which enhance guest–host interactions.<sup>62–65</sup> Moreover, from a practical perspective, incorporating AIEgens into MOFs offers several distinct benefits, as follows:

1. The photonic characteristics and electron excitation energies of AIEgens, such as wavelength, emission color, and bandgap, can be readily modified by changing the organic ligands or metal ions to suit practical application needs.
2. The inflexible structures and particular arrangements derived from reticular chemistry can effectively restrict intramolecular vibrations, rotations, and movements, avoiding self-quenching and markedly enhancing the luminescence efficacy.
3. The ultra-porous characteristics, customizable internal chemical atmosphere, accessible canals, and modifiable cavity dimensions and geometry of these frameworks allow guest moieties to engage completely and explicitly with the AIEgen attached with the system, resulting in a notable enhancement in detection capabilities.<sup>11</sup>

Due to dedicated research efforts, numerous innovative AIE systems have been created, with diverse mechanistic aspects and several practical uses. However, previous reviews broadly discussed AIE and AIE-MOFs across multiple domains, and thus this review provides a distinct focus on the mechanistic strategies for converting ACQphores into AIEgens and their structural impact on emissive behaviours. Herein, this review begins by thoroughly explaining the principles of the AIE and ACQ phenomena, along with the mechanistic understanding obtained from both theoretical models and investigational data. Further, an illustration of how traditional ACQphores have been transformed into new AIEgens is provided, followed by a discussion on the advancement of AIE-based MOFs. Rather than covering all possible applications, this review is specifically organized around the sensing applications of AIE-MOFs. Hence, a detailed examination of their sensing applications will be discussed for detecting various substances such as VOCs, nitroaromatics, biological entities, heterocyclic compounds, and heavy metals in water, as well as the design of stimuli-responsive luminescent materials and optoelectronic devices (Fig. 1).

## 2. Emission and quenching

AIE is a photochemical effect associated with the clustering of chromophores. The term AIE was presented by Tang & team in 2001, demonstrating the emission behaviour of silole, thus marking a significant advancement in the field of luminescent emission.<sup>12</sup> This group noted a luminescence emission pattern that contradicted the typical ACQ. In contrast to ACQ compounds, AIE compounds show significant emission in their accumulated/aggregated or solid form, while otherwise showing little emission in diluted systems, which is called

AIE.<sup>14</sup> An enhanced comprehension of AIE mechanisms can help in controlling light emissions for beneficial purposes, while avoiding harmful effects. Further, the luminogen moieties can be specifically engineered for advanced technological applications, achieving improved performances and minimizing shortcomings, rather than relying on luck. Several studies have been proposed to clarify the AIE mechanism,<sup>90</sup> among which the restriction of intramolecular motion (RIM) theory,<sup>91–93</sup> viz., the limitation of intramolecular rotation and vibration,<sup>15,94</sup> is broadly recognized as one of the most acceptable interpretations. Here, the discussion will be focused on the fundamental principles of the AIE mechanism and further recognizing that dynamic intramolecular movements can efficiently release exciton energy, and restricting these movements (RIM) can trigger radiative transitions.

### 2.1. Mechanistic insights

Molecular movements, such as rotation and vibration, require energy. In dilute solutions, intramolecular rotations occur, leading to energy loss from the electronically excited states through non-radiative decay pathways. In contrast, when in the aggregated state (in concentrated solutions), these rotations are limited by physical constraints, preventing non-radiative relaxation and allowing excitons to decay through radiative processes.<sup>13,95–98</sup> Typically, the AIE phenomenon arises from the limitation of the within-molecule movement, which encompasses both the limitation of intramolecular vibrations and rotations.<sup>15</sup>

Tang *et al.* categorized luminescence pathways into various types based on molecular structure (Fig. 2).<sup>91</sup> Molecules with a propeller shape, such as hexaphenylsilole (HPS) and tetraphenylethene (TPE), exhibit AIE activity due to the suppression of internal molecular rotation by the RIR process. Alternatively, 10,10',11,11'-tetrahydro-5,50-bidibenzo[*a,d*][7]annulenyldiene (THBA)<sup>99</sup> has a core-shell structure and possesses phenyl rings connected by a flexible bend. This flexibility allows it to vibrate dynamically in solution, which significantly reduces photon emissions.<sup>15</sup> In THBA, its alkene chains and phenyl rings are linked by covalent linkages, creating an extensive  $\pi$ -conjugated framework, as shown by the yellowish circle in Fig. 2. As a result, the structural foundation of luminogenic chromophores is established by through-bond electronic conjugation. Recently, some unconventional luminogens that lack traditional photoactive units or through-bond (covalent) conjugations have been discovered to exhibit significant AIE behaviour.<sup>15</sup> For instance, (*R*)-diethyl-1,2,3-triphenyl-1,2,3,6-tetrahydropyrimidine-4,5-dicarboxylate (THP) does not emit any light when in solution.<sup>100</sup> In solution, the movement of its aryl and ester groups, along with the vibrational dynamics of its tetrahydropyrimidine moiety and carbonyl linkages, suppresses the photoluminescence from its fluorophore. However, THP crystals emit light effectively due to RIM occurring in organized clusters. In the case of *o*-BP-TPE, electronic interactions occur *via* spatial interactions, creating a conjugated fluorophore, as denoted by the pink rectangle in Fig. 2. Recently, it has been discovered that luminogens with one or more carbonyl units

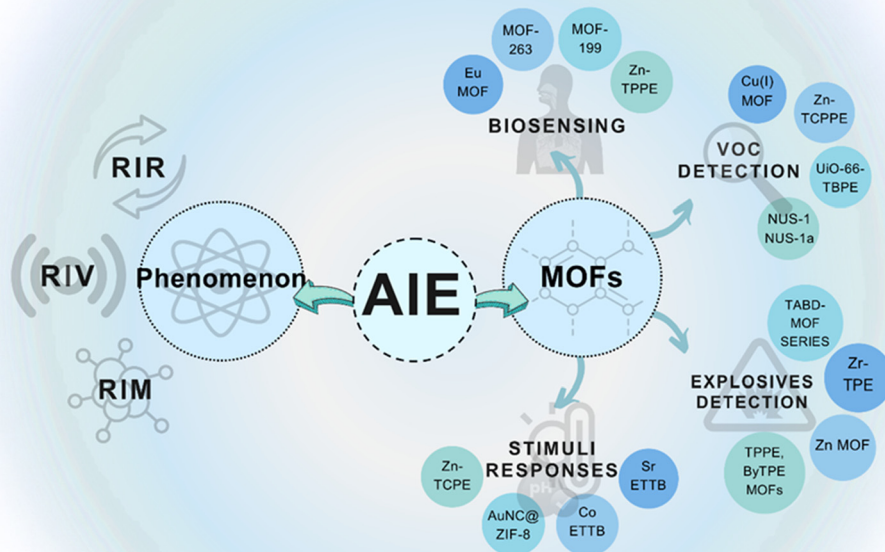


Fig. 1 Chart showcasing the phenomenon responsible for the AIE effect in MOFs and several sensing applications of AIE-MOFs in various fields.

display crystallization-activated phosphorescence when exposed to ambient heat.<sup>15</sup> For example, benzil crystals exhibit phosphorescence because their numerous carbonyl groups facilitate effective intersystem crossing.<sup>101</sup> Covalent intramolecular electronic interactions occur inside individual benzil molecules (indicated by the yellowish rectangle), as well as spatial intermolecular  $\pi$ -conjugation among distinct benzil molecules (as shown in the pink coloured rectangle). In the solvent phase, the phosphorescence of benzil is diminished due to the dynamic vibrations of its carbonyl group and the rotation of its phenyl group; however, in the crystalline phase, this molecule exhibits efficient phosphorescence. These two types of electronic conjugation provide benzil crystals with AIE activity, which is linked to the RIM process triggered by the non-covalent interactions between its moieties in the frozen state during crystallization.

According to Tang and colleagues, the RIR phenomenon is accountable for the AIE mechanism.<sup>9</sup> This team performed several control experiments, such as exerting pressure, redu-

cing the temperature, and increasing the viscosity, to externally trigger the RIR process. Further, they utilized covalent linkages to attach aryl rotating units, initiating the RIR mechanism at the molecular scale. As a result of both external and internal stimuli, the luminogens exhibited emission. In the literature, various types of luminogenic molecules have been developed by structurally designing conjugated anchors equipped with several aromatic side rotating units.<sup>22–26</sup> For example, one of the earliest derivatives of silole, hexaphenylsilole (HPS), is a non-planar, propeller-shaped unlike the traditional planar disc luminophores such as perylene. This structural distinction leads to differences in their emission properties. In dilute medium, the six phenyl rotating units of the HPS moiety engage in internal rotational dynamics around its silacyclopentadiene or silole nucleus, which dissipates its electronically excited state *via* non-radiative decay, resulting in a lack of luminescence. Alternatively, in aggregated form, the HPS moiety cannot align *via*  $\pi$ - $\pi$  stacking mechanism owing to its propeller-like conformation, and the internal rotations of the



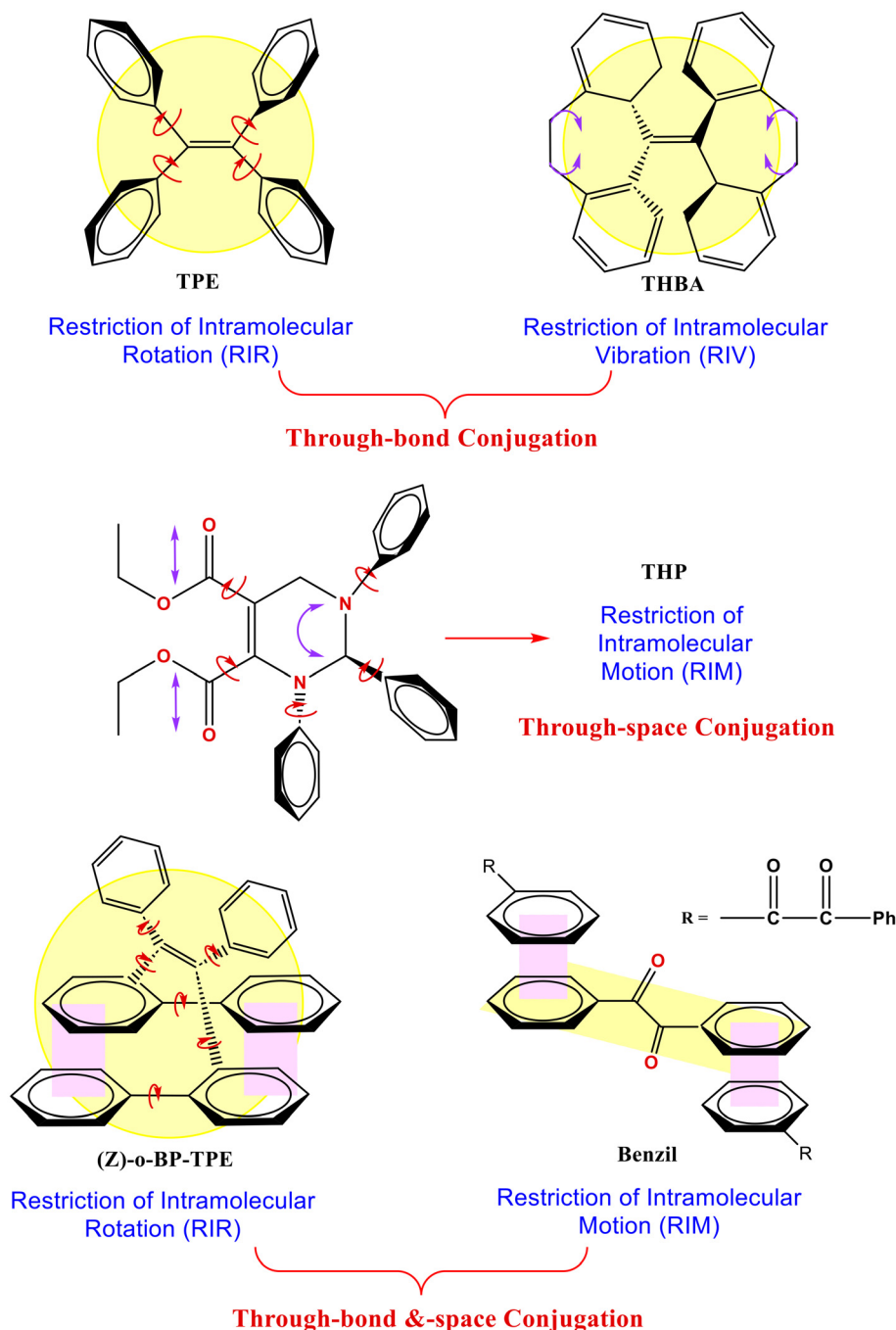


Fig. 2 Classification of AIEgens based on their molecular structures.

aryl moieties are significantly limited by spatial restrictions. This constraint of intramolecular rotations (RIR) prevents the non-radiative decay and facilitates the emissive pathway. Consequently, the HPS moieties exhibit emission in their accumulated state.<sup>13</sup> Alternatively, with recent progress in AIE research, newer AIEgens, such as THBA, do not emit based on the RIR phenomenon.<sup>99,102</sup> THBA lacks rotatable units due to its phenyl rings being constrained by two ethylene tethers, although it demonstrates AIE due to RIV, as shown by Tang

and colleagues.<sup>14</sup> Given the fact that rotational motions use energy, it is expected that vibrational motions would also behave in a similar manner. Thus, it was found that THBA does not show emission in the solution phase, while it exhibits intense photoluminescence in aggregate form. Additional studies confirmed that the vibratory movements of the attached phenyl rotors are responsible for the consumption of excitation energy.<sup>99</sup> Moreover, quantum/molecular mechanics (QM/MM) modelling outcomes showed that standalone THBA

(such as in dilute solution phase) exhibits six fundamental vibrational modes, which significantly utilize excited-state energy, resulting in inefficient emission. In contrast, when THBA is in the aggregated state, only three normal vibrational modes are responsible for substantial excited-state energy consumption. Thus, the reduction in the number of vibrational modes and decrease in exciton energy consumption by 30% due to RIV in the aggregations allow THBA to undergo radiative decay to show AIE. Therefore, it is evident that either RIR or RIV can contribute to the AIE effect. If both RIR and RIV are present in a system, which is collectively termed RIM, where motions (M) including vibrations (V) and rotations (R), the luminogen is guaranteed to be AIE active. Thus, AIEgens having an oscillatory core and rotational peripheral components can be interpreted using the RIM mechanism.<sup>103–106</sup> For example, a phenothiazine derivative, PTZ-BZP (1), adopts a nonplanar, butterfly-shaped molecular structure, as shown in Fig. 3, which is supported using the DFT-augmented ground-state configuration (B3LYP/6-31G-(d,p)).<sup>103</sup> It does not emit light in solution, while it produces intense red emission in THF/water blends. Here, the phenothiazine scaffold is adorned with movable phenyl and benzothiadiazole rings. The DFT-optimized structure revealed that the phenothiazine scaffold has a bent molecular configuration. In its isolated state, there are two primary non-radiative pathways that dissipate its excitation-state energy, as follows: (i) the rotating movements of the phenyl and benzothiadiazole rings and (ii) the vibrating movements of the phenothiazine scaffold. When aggregates are formed, they restrict the internal dynamics of the rotational and oscillatory components, resulting in luminescence.

## 2.2. From ACQ to AIE

ACQ was identified by Förster in 1954 while considering the concentration-dependent deactivation of emissions.<sup>28</sup> Moreover, it is widely acknowledged that numerous aromatic luminophores experience the ACQ effect, as also noted by Birks in his seminal 1970 book, "Photophysics of Aromatic Molecules".<sup>10</sup> Traditional luminophores typically emit light intensely as individual molecules, but they experience different levels of ACQ naturally in the aggregated state. The ACQ effect is quite prevalent, and is also noted in inorganic photonic frameworks, including quantum dots.<sup>10,107,108</sup> In

terms of practical use, it tends to cause more harm than benefit in many situations.<sup>109–113</sup> Due to the negative impact of the ACQ effect on practical applications, various research teams have worked extensively to address this issue. Typical strategies involve employing chemical transformations, physical techniques, and engineering approaches to prevent the aggregation of luminophore species.<sup>114–118</sup> For example, large ring-shaped moieties are added to luminophores and optically clear polymeric units are mixed with them to prevent them from getting too close to each other.<sup>9</sup> However, using these electronically non-conjugated materials can lead to a reduction in the extent of conjugation and a decrease in OLED efficacy due to the twisting of the chromophore structure and obstacles in charge mobility.

In recent years, numerous studies have focused on converting ACQphores to AIEgens, which retain the required characteristics of traditional luminophores, while also benefiting from the AIE property. In this context, as discussed earlier, Tang and colleagues<sup>14</sup> identified two main factors that influence the AIE property. The first factor involves moieties capable of undergoing dynamic internal motions that effectively release excitation energy in discrete states. The second factor pertains to the twisted three-dimensional configurations in clustered states, which successfully inhibit harmful aromatic stacking interactions. Therefore, incorporating these AIE components into ACQ structures can serve as a viable strategy to convert ACQphores to AIEgens. This discussion will review a collection of studies on the conversion of ACQ to AIE, emphasizing the achievements and insights gained. Before delving into the techniques for ACQ to AIE conversions, a quantitative parameter, also known as the  $\alpha$  factor, is defined here, which is used to quantify the variation in luminescence efficacy from the solution to the aggregated phase, as shown below:<sup>9</sup>

$$\alpha = \frac{\varphi_{F,a}}{\varphi_{F,s}}$$

where  $\varphi_{F,a}$  represents the quantum yield of fluorescence for aggregates (this value can be replaced by  $\varphi_{F,f}$  or  $\varphi_{F,c}$ , if the aggregates are confirmed to be in the form of an amorphous thin film or crystalline solid, respectively). According to this definition, if the  $\alpha$  parameter for a luminophore exhibiting AIE functionality ( $\alpha_{AIE}$ ) is greater than 1, it indicates a strong AIE impact. Alternatively, if the  $\alpha$  magnitude for a fluorophore having ACQ characteristics ( $\alpha_{ACQ}$ ) is less than 1, it shows a significant ACQ effect. The conversion processes of ACQ to AIE have been further divided into three primary categories, as follows: (i) improving ACQphores through the integration of AIEgens, (ii) substituting parts of AIEgens with ACQ components, and (iii) developing innovative AIEgens from ACQphores using the RIM concept.

**2.2.1. Improving ACQphores through the integration of AIEgens.** Significant efforts have been dedicated to converting the ACQ-responsive triphenylamine (TPA) to AIEgens.<sup>119–122</sup> The TPA scaffold was modified by conjugating three and one unit of tetraphenylethene (TPE) to the TPA core, resulting in 3TPE-TPA (2)<sup>119</sup> and TPE-TPA (3),<sup>120</sup> respectively. Further, two

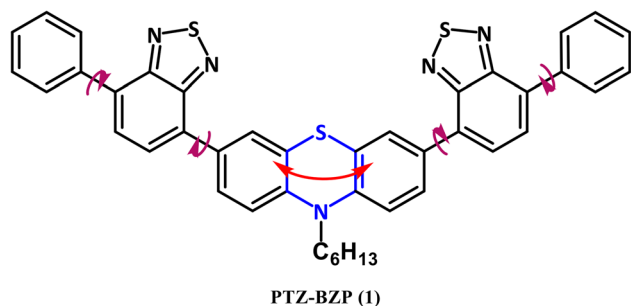


Fig. 3 Representative AIEgen explained by the RIM principle.

TPA cores were connected to one TPE in TPE-2TPA (4), as shown in Fig. 4.<sup>120</sup> Here, all three molecules exhibited the combined advantages of TPA, resulting in the ability to transport holes, and TPE units for AIE activity. Compounds 2, 3, and 4 show low solvated-phase  $\Phi_{\text{FS}}$  of 0.42%, 0.38%, and 0.24%, while their solid-state film  $\Phi_{\text{FS}}$  are significantly higher at 92.0%, 100%, and 100%, respectively. Moreover, as the ratio of TPA to TPE increases, the peak emission shifts to longer wavelengths of 484, 486, and 505 nm for compounds 2, 3, and 4, respectively. This bathochromic shift in luminescence can be attributed to either the enhanced electron-releasing characteristics of the TPA unit or the increased electronic delocalization throughout the compound. In addition to TPE, other AIEgens such as triphenylacrylonitrile (TPAN) can also be employed for similar applications.<sup>121,123</sup> The proportion of TPAN to TPA could be methodically adjusted from 3 : 1, to 2 : 1, to 1 : 1 to form novel adduct moieties, 3TPAN-TPA (5),<sup>121</sup> 4TPAN-2TPA (6),<sup>121</sup> and TPAN-TPA (7), as shown in Fig. 4.<sup>123</sup> Compounds 5, 6, and 7 exhibited AIE activity. In THF, their fluorescence quantum yields ( $\Phi_{\text{FS}}$ ) were recorded to be 0.23%, 0.48%, and 1.62%, while in the solid phase, their  $\Phi_{\text{FS}}$  increased to 33.2%, 38.2%, and 99.0%, respectively. The effective transition from aggregation-caused quenching to aggregation-induced emission in these instances can be

described analogously to earlier systems, where the movement of the phenyl rings in the attached AIEgens dissipates the excited-state energy, while subsequent restriction of these movements activates the emission. Due to their high emission in the solid state and effective hole-conducting characteristics, they were utilized in OLEDs, where these types of compounds are applied as emissive layers and hole-conducting layers, demonstrating an exceptional performance.

A common nitrogen-bearing ACQphore, that is carbazole, has likewise been methodically modified by AIEgens, such as TPE.<sup>122,124,125</sup> Modifying 9-octyl-9*H*-carbazole (Cz) with different amounts of TPE units gives TPE-carbazole adducts. These adducts are AIE active, and their  $\Phi_{\text{FS}}$  improved from the solution-state range of 0.18% to 0.37% to film-state of 44.6% to 61.1%. This was further advanced with an increase in the number of TPE substituents due to the decrease in the solubility of these adducts in the THF/water system, leading to their early aggregation. Thus, the formation of aggregates subsequently triggers radiative decay through the RIM process. Further, the carbazoles were also modified at the nitrogen centre by TPE to be transformed into AIE-active compounds, while varying the TPE to carbazole ratio. It was noted that when TPE is linked to the nitrogen atom, the emission maximum is more blue-shifted as compared to that where TPE

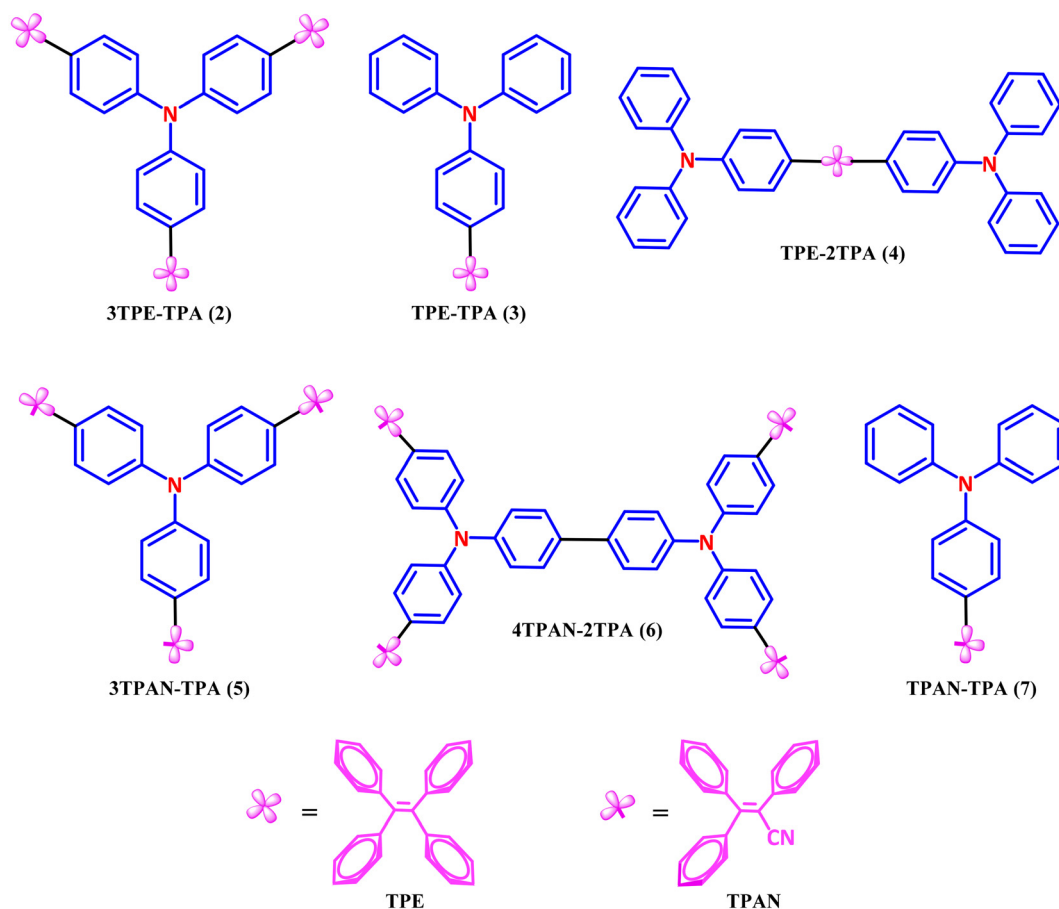


Fig. 4 Examples of ACQphores integrated with AIEgens (TPE and TPAN).

groups are connected to the carbon atoms on the aromatic rings of carbazole, suggesting a decrease in the electronic delocalization efficacy through the N-linkage. In addition, the N in carbazole was replaced with S or O, such as in dibenzothiophene and dibenzofuran, which was then combined with the AIEgen triphenylethene, TPEH (8) to create TPEH-3BFu (9) and TPEH-3Bt (10), respectively.<sup>126</sup> Both compounds 9 and 10 exhibit significant emission in their accumulated state, showing quantum yields ( $\Phi_{\text{Fs}}$ ) of 19.0% and 22.0%, respectively. Here, it is important to highlight that the compact planar ACQphores might function as rotating units, facilitating the dissipation of energy in the excited state. Although in 9 and 10 their nonplanarity arises from TPE (Fig. 5), which prevents intermolecular aromatic  $\pi$ - $\pi$  interactions, and also combined with RIM, this leads to effective emission in the aggregate state. Furthermore, numerous other studies have been conducted beyond those mentioned,<sup>127–133</sup> each of which has effectively converted ACQphores into AIEgens. As anticipated, the resulting ACQphore-AIEgen adducts frequently manage to combine the strengths of both components, leading to a positive synergy.

### 2.2.2. Substituting parts of AIEgens with ACQ components.

In addition to the alteration of ACQphores by attaching AIEgens, the further modification of traditional AIE blocks *via* the integration of ACQ-phoric blocks was considered a potential strategy for advancing novel AIE-functionalized frameworks. This strategy aimed to preserve the inherent AIE activity of the AIEgenic cores while simultaneously integrating the functional characteristics of ACQphores and mitigating their quenching effects. For instance, the substitution of one aryl group in TPE with spirobifluorene (SF) gives TPE-SF (11), as shown in Fig. 6.<sup>125</sup> Here, the clustered-state aromatic stacking interactions and luminescence suppression have been mitigated by the significantly contorted conformation originating from the propeller-like TPE precursor. In a solvated environ-

ment, the movement of the phenyl units leads to luminescence suppression; however, in the aggregated phase, these motions are prohibited, resulting in the activation of emission through the RIM effect. Similarly, TPA and carbazoles were functionalized on TPE to synthesize AIE-active compounds 12, 13, and 14, as illustrated in Fig. 6.<sup>134</sup> It is noteworthy that substituting a single phenyl unit of TPE by a carbazole unit, whether through a C-C or C-N linkage, results in AIE-active carbazole derivatives.

Similar to the retention of the AIE property observed with the substitution of one phenyl ring in TPE, the replacement of two phenyl rings can also yield novel AIE-active compounds, such as diphenylfumaronitrile, 15 (Fig. 6). Additionally, fluoranthene molecules were employed to substitute the TPE units in an effort to mitigate the ACQ impact in compound 16.<sup>135</sup> As anticipated, compound 16 exhibits characteristic AIE behaviours, demonstrating a notable enhancement in emission in THF/water mixtures. Here, the suppression of luminescence in the solution is likely accredited to the internal rotational motions of the peripheral phenyl and fluoranthenyl rings. When in the aggregated state, the propeller-like conformation of compound 16 hinders close  $\pi$ - $\pi$  stacking interactions, which further obstructs the generation of excimer complexes, thereby reducing ACQ.

Further, systematic investigations were conducted to methodically substitute phenyl rings in TPE with naphthalene rings, resulting in the development of a range of novel AIE-active compounds, such as NTPE (naphthyltriphenylethene, 17), DNDPE (dinaphthyltriphenylethene, 18), TNPE (trinaphthyltriphenylethene, 19), and TNE (tetranaphthyltriphenylethene, 20) (Table 3),<sup>136</sup> exhibiting AIE properties. Here, the naphthalene moieties also function as rotors. In addition, the progressive substitution of phenyl rings with naphthyl units results in an upsurge in conjugation, which subsequently induces red shifts in both the emission and absorption spectra of these com-

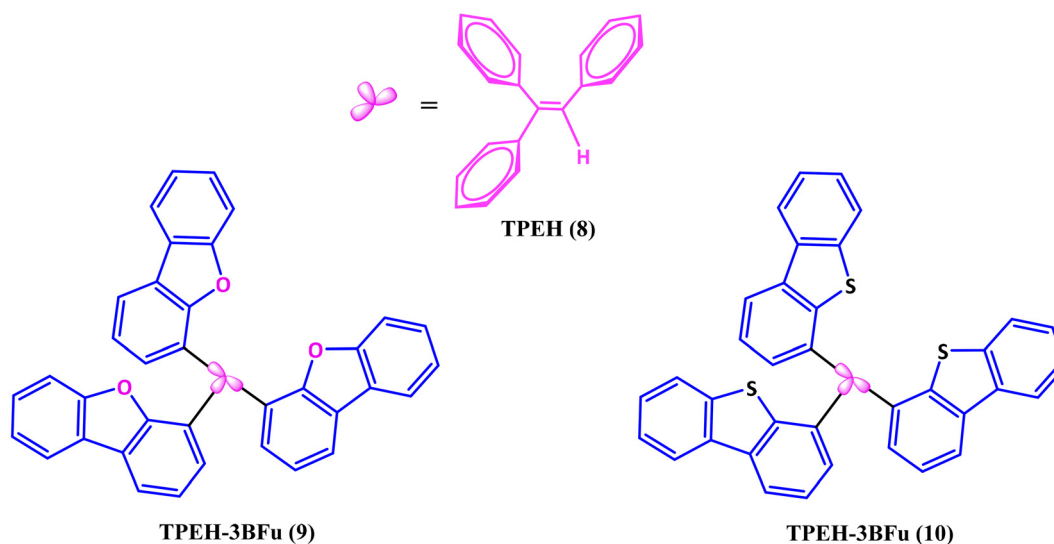


Fig. 5 Examples of ACQphores integrated with an AIEgen (TPEH).



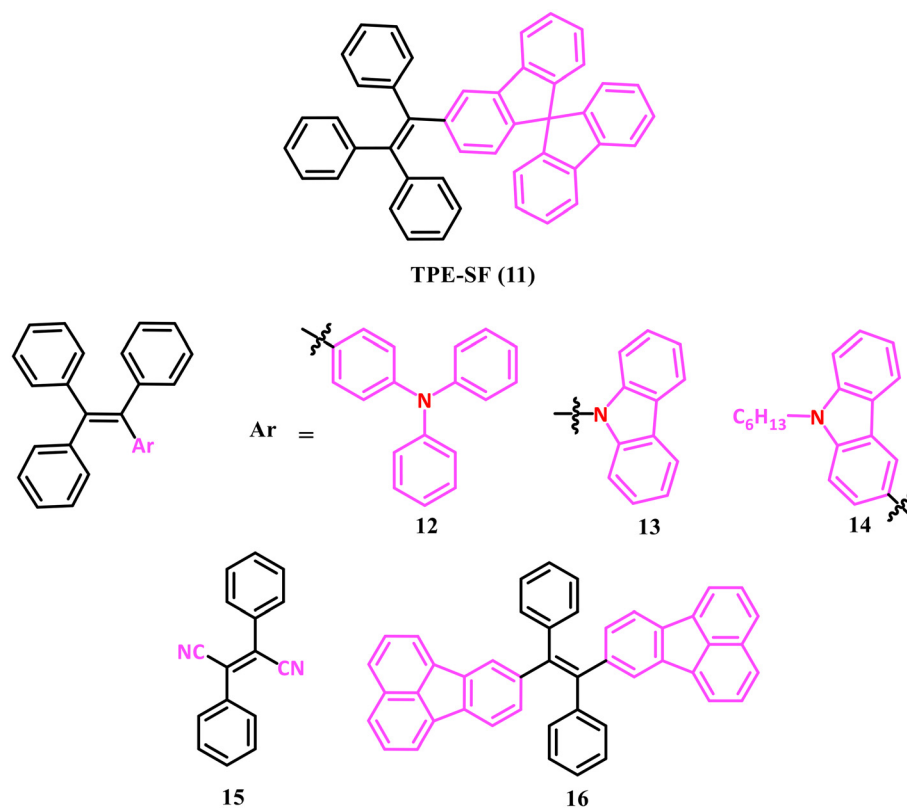


Fig. 6 Replacement of parts of AIEgens with ACQphores.

pounds. In TPE, the presence of smaller aromatic rings facilitates rotational motions, which efficiently release the excitation energy. Conversely, the larger naphthyl groups exhibit less energy dissipation, as evidenced by the slight increase in the fluorescence quantum yield ( $\Phi_{\text{FS}}$ ). Furthermore, due to their size, which is twice as large as TPE, the flat naphthyl units are more susceptible to forming internal molecular aromatic  $\pi$ - $\pi$  interactions. When in solid phase, the naphthyl units from adjacent moieties may partially coincide, leading to significant  $\pi$ - $\pi$  interactions, and consequently a decrease in emission intensity. The potential for analogously developing new AIE compounds by substituting the phenyl cores of luminogens with aggregation-causing quenchers has additionally been substantiated by studies on further representative luminogens, including DSA (9,10-di((*E*)-styryl)anthracene),<sup>137</sup> diphenylfumaronitrile,<sup>138</sup> and silole.<sup>139–141</sup> Systematic studies have demonstrated that excessive modifications to the AIE scaffold might adversely impact its AIE behaviour, potentially influencing both its solid and solution phase emissions, and in some instances, affecting both states simultaneously.<sup>136,137,141</sup> Therefore, several additional challenges must be addressed prior to formulating precise guidelines for this substitution strategy.

**2.2.3. Developing new AIEgens from ACQphores.** Based on the AIE mechanism and the previously discussed research, it can be inferred that the fundamental principle underlying the conversion strategies from ACQ to AIE involves the incorpor-

ation of adequate motional elements and nonplanarity. Consequently, it is reasonable to expect that any methodology aligning with this principle should be effective. Therefore, the synthesis of novel luminogens from luminophores and non-AIE constituents is indeed feasible. Numerous examples exist to substantiate this assertion.

As illustrated in Fig. 7, a novel series of AIE composites was synthesized by linking aromatic rotors and stators through flexible single bond linkages. This modification allows the loss of excitation energy through rotational motions in the solution phase. However, more significantly, in the clustered state, these dynamics are restricted, leading to excitation-state relaxation *via* dissipative processes. Furthermore, the nonplanar configurations resulting from the torsional motion characteristics of the linked aromatic moieties may inhibit close  $\pi$ - $\pi$  stacking among the luminogens, thereby preventing luminescence suppression in the clustered phase. Initially, an individual phenyl moiety was affixed to a micro ACQphore, *i.e.*, isothiazolo[5,4-*b*]pyridin-3(2*H*)-one (ITPO), resulting in **21**.<sup>142</sup> Given that the rotating motions of the ITPO unit and the phenyl ring deplete the excited-state energy, **21** exhibits nearly no emission in the solution phase. Alternatively, an intense blue luminescence with  $\Phi_{\text{F}}$  of 28.0% was seen in its aggregate state, exhibiting the AIE characteristic of **21** due to RIM. Furthermore, a comparable system, **22**, was developed by adding two rotatable phenyl rings to quinoline.<sup>143</sup> In its excited state, the quinolone and two phenyl rings effectively

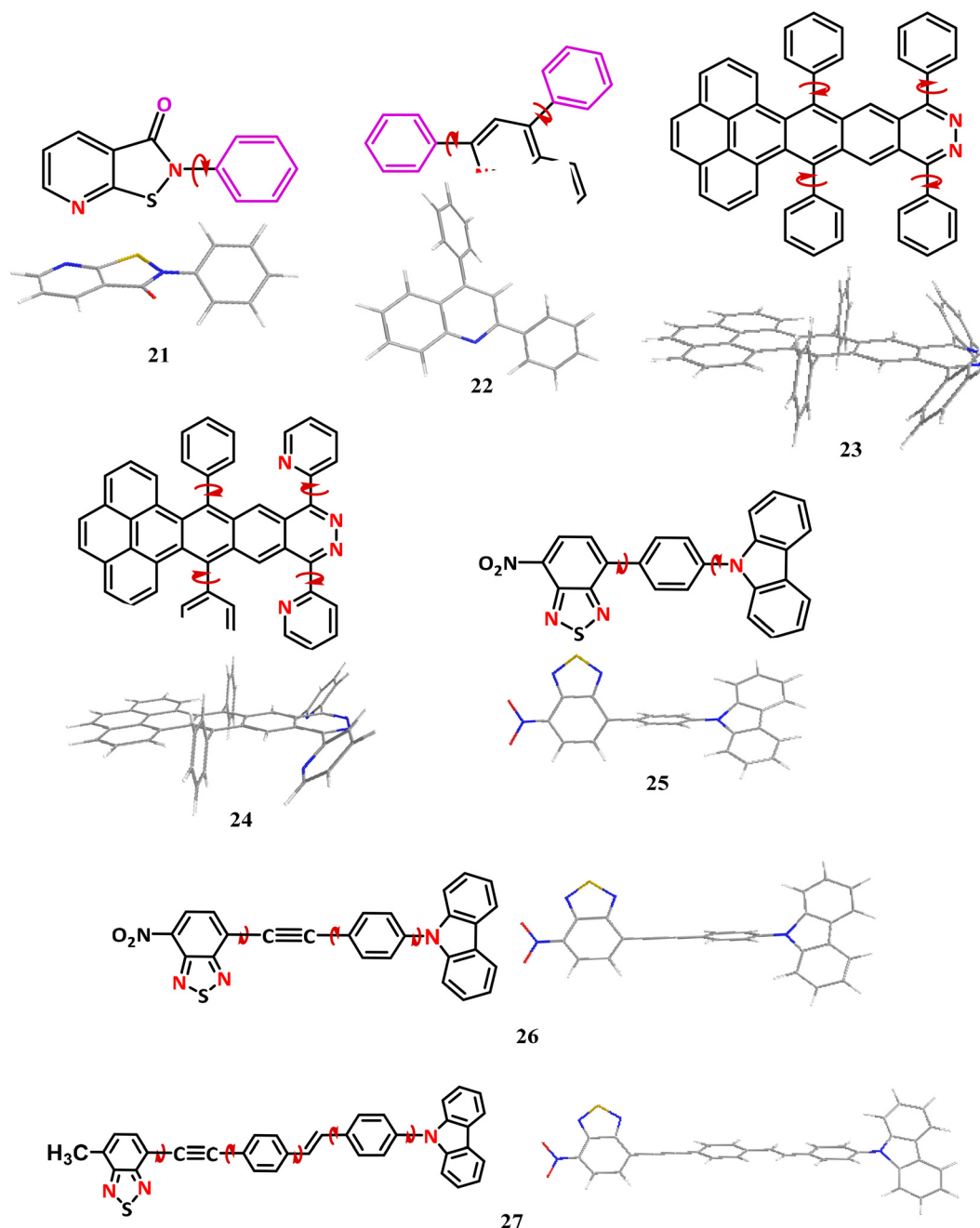


Fig. 7 Examples of AIEgens developed from the decoration of ACQphores with aromatic rotors.

use excitation-state energy through rotational motion, while emission is evident when these movements are stopped in the solid phase. In addition, four rotating aromatic moieties were used to adorn the quite larger pentacene analogue in compounds 23 and 24, which are AIE active.<sup>144</sup> The inactive solution-state of these compounds were converged to emission active as radiative decay took over when the rotational movements of the four rings were compromised in the accumulated phase. Moreover, their heavily contorted 3D conformation also contribute to preventing  $\pi$ - $\pi$  stacking and production of excimer complexes, thereby aiding in luminescence.

Furthermore, the ACQ-to-AIE transformation was also carried out by the single-bond coupling of luminophores, in addition to the tactic of affixing rotatory aromatic rings to ACQphores. Compounds 25, 26, and 27, which exhibit typical AIE activities, were obtained by singly bonding nitril, benzothiadiazole, phenyl, and carbazole, as shown in Fig. 7.<sup>145,146</sup> Here, the aromatic species tilt out of plane with regard to each other based on their type of moieties, as can be seen from their crystal structures. The twisted nonplanar conformation indicates a relatively weak conjugation between the aromatic units. In the end, it helps with the luminescence suppression

in the solvated state by permitting rotating motions when the moieties are unbound. Conversely, RIR activates the luminescence in the solid phase. It is simple to create AIE-active compounds having orange or even crimson luminescence by joining these aromatic moieties that donate electrons and those that withdraw electrons through single-bond linkages. To create novel AIE compounds, bulkier aromatic units can also be individually joined by single bonds.<sup>147–149</sup>

**2.2.4. New AIEgens including TPA units.** Recently, novel luminogens were developed by incorporating the TPA unit due to its electron-releasing behaviour. Thus, newer products with TPA can be generated by using the D–A (donor–acceptor) geometry when electron-deficient (electron-acceptor) moieties are attached to it. This results in unique properties in the products such as solvato-fluorochromism and biphotonic absorption or biphotonic-induced fluorescence.

For example, blue 28, green 29, and yellow 30 luminogens were readily synthesized by incorporating TPA with imidazolium, pyrimidine, and malononitrile moieties, respectively (Fig. 8).<sup>150–152</sup> The numerous rotating units in 28, 29 and 30 facilitate the dissipation of excitation energy through rotating movements in the solution phase. However, during their accumulation, these dynamics become restricted, leading to

the activation of emission. As indicated by the crystal structure of 28 and the adjusted configurations of 29 and 30, the non-planarity of these compounds, resulting from the single bond connections between aromatic components, helps avoid unwanted  $\pi$ – $\pi$  stacking, thereby enhancing their emission efficiency in the aggregate state. Additionally, several starburst multi-branched TPA frameworks having D– $\pi$ –A– $\pi$ –D configurations have been identified as AIE-active compounds.<sup>153–157</sup>

Furthermore, TPA-based quadrupolar analogues 31a and 31b were developed by utilizing vinyl bridges extending from a dicyanobenzene centre, where TPA units serve as junctions for phenothiazine or diphenyl amine, respectively, as shown in Fig. 9.<sup>153</sup> Moreover, using a comparable strategy, starburst TPA analogues 32a and 32b were also synthesized.<sup>154</sup> These four molecules exhibit minimal emission when solubilized in THF but emit sharp red fluorescence in the accumulated phase, demonstrating characteristic AIE behaviour. Due to the interconnected multi-D–A organization, these compounds also possess high biphotonic uptake cross-section data and effective two-photon excited fluorescence (TPEF) in the accumulated phase, turning them into potential candidates for bio-optical utilization.

Thus, this segment explored novel luminogens that integrate TPA motifs into their molecular frameworks, leveraging

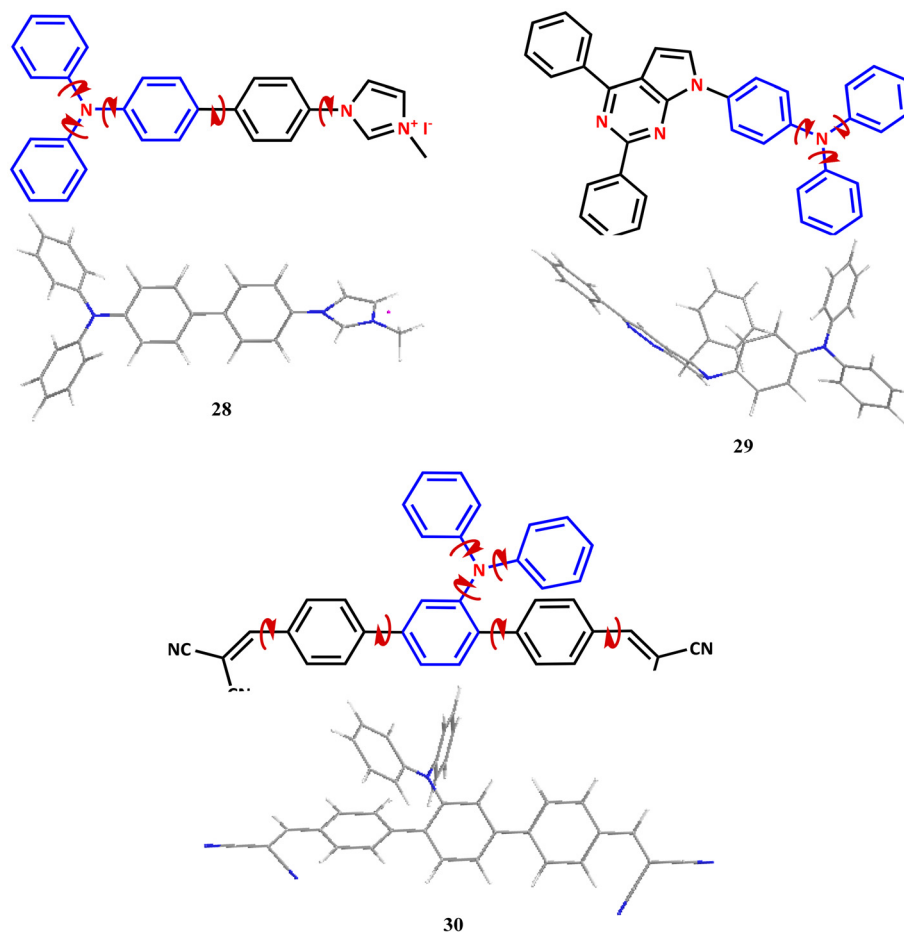


Fig. 8 Conversion of ACQphores into AIEgens by attachment of triphenylamines to  $\pi$  moieties.

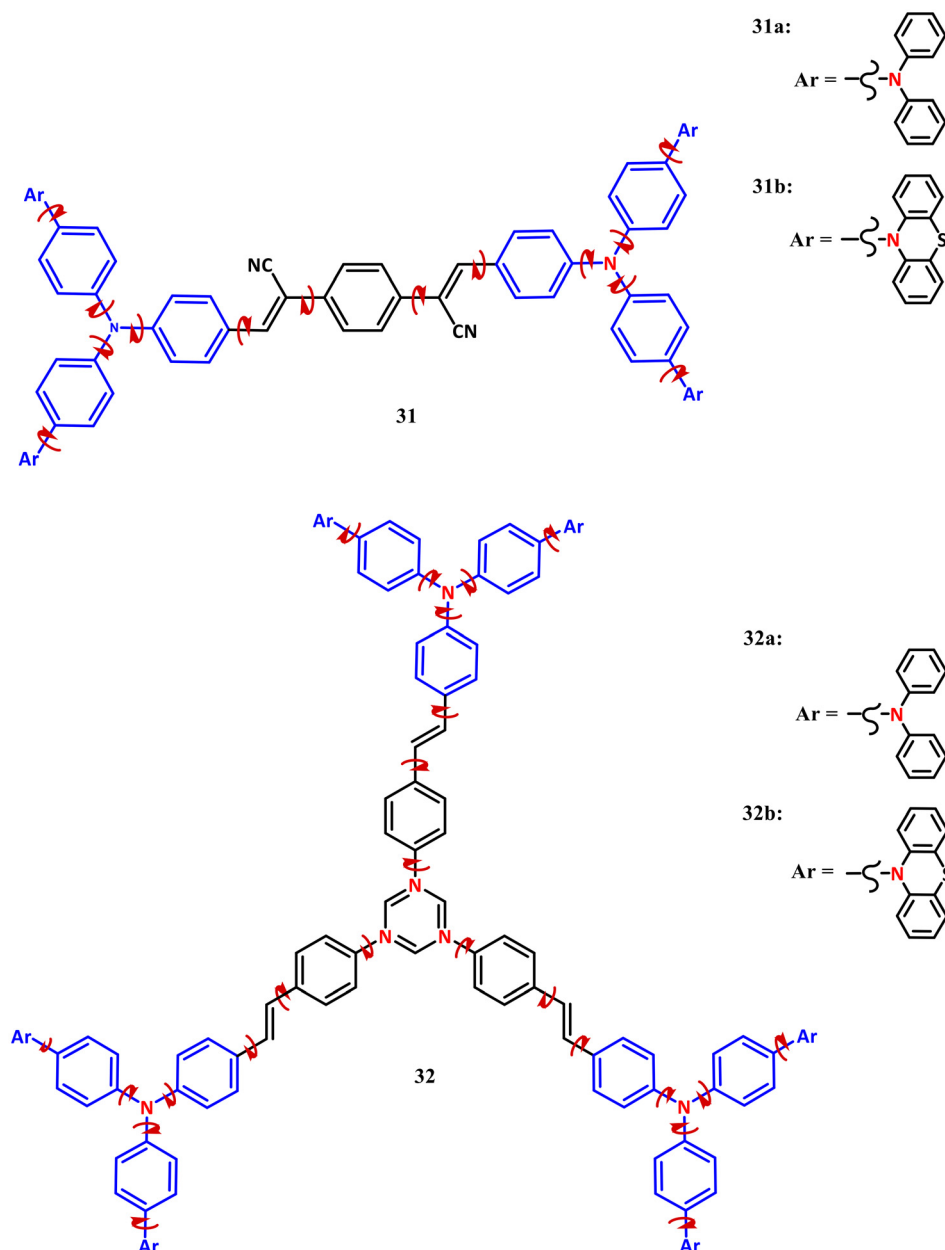


Fig. 9 Conversion of ACQphores into AIEgens having starburst structures by the attachment of triphenylamines to  $\pi$  moieties.

the numerous phenyl moieties and contorted 3D configuration of the TPA fragment. The incorporation of TPA illustrates how AIEgens can be designed, while retaining desirable characteristics from ACQphores. Thus far, we have thoroughly analyzed the mechanisms and processes governing ACQ and AIE, along with the methodologies developed to alter ACQ-active molecules into AIEgens.

In the following section, we will shift our attention to recent research on MOFs incorporating AIE-active components. We will discuss their development, characterization, and relevant studies, along with their applications in sensing technologies.

### 3. AIE-MOFs in sensing applications

Chemically tunable MOFs with porous structures are supremely promising for sensing applications because they offer significant advantages in sensitivity and selectivity, which are the two major performance parameters in fluorescence-based chemical sensing. Further, high selectivity towards certain analytes can be attained by strategically modifying the inner surfaces of MOFs with tailored chemical functionalities. Additionally, MOFs with large surface areas and adjustable internal environments provide abundant adsorption and binding sites, enhancing the sensitivity by interacting with the

desired analytes. Due to the inherent properties of AIEgens, the fluorescence quantum yield of AIE-MOFs can be finely adjusted from nearly unity to almost non-fluorescent. Moreover, the presence of guest molecules can significantly affect the rotational dynamics of the phenyl rings inside AIE-MOFs, enabling them to function as highly effective “turn-off” or “turn-on” sensors. This section highlights the diverse applications of AIE-MOFs in various sensing technologies, including limited the detection of volatile organic compounds (VOCs), nitroaromatics and heterocyclic compounds, and biological molecules, and further as stimuli-responsive luminescent materials.

### 3.1. Sensing of biological moieties

Biomarkers, such as proteins, amino acids, and metal ions, are amongst the specific molecular entities that can be identified or quantified in samples collected from an organism or its external environment.<sup>158,159</sup> By measuring and analysing these biomarkers, essential biological insights and diagnostic information can be acquired. In medicine, biomarkers are widely used for early disease detection, prognosis assessment, treatment monitoring, and other applications. These are crucial in improving the diagnostic accuracy and enhancing the efficacy of personalized therapies. AIE materials have been found to be significantly utilized in targeted drug delivery, therapy monitoring, photothermal and photodynamic treatment strategies, detection of biomolecules, as well as in cellular and *in vivo* imaging, thereby advancing the field of precision medicine.<sup>160</sup>

Yin and colleagues developed an AIE-active Eu-based MOF using the ligand tetrakis(4-carboxyphenyl)pyrazine, which exhibited intense dual emissions from both  $\text{Eu}^{3+}$  ions and the ligand.<sup>161</sup> The Eu-MOF effectively and selectively detected arginine through ratiometric luminescence in the concentration range of 0–160  $\mu\text{M}$ . Further, the structural determination revealed that molecules of arginine having suitable dimensions could enter the pores of the MOF, where several hydrogen bonds were formed between the nitrogen atoms of the ligand with the guanidyl groups present in arginine. These hydrogen bonds, along with the incorporation of arginine, constrained the movement of the phenyl rings present in the ligand, thereby extending the conjugation length and enhancing the blue emission. At the same time, these bindings did not interfere with the ligand-to- $\text{Eu}^{3+}$  antenna effect, preserving the stability of the red emission, which acted as a reference point for ratio-based sensing. Remarkably, the color change from red into blue, corresponding to increasing arginine levels, was clearly visible to the naked eyes, thus representing a simple approach for the detection of arginine (Fig. 10).

Recently, Li and colleagues developed a dual-functional Zn-MOF, namely LMOF-263, using a mixed-ligand approach. They incorporated pyridyl-adorned TPE units as the source of luminescence and sulfone-functionalized ligands as coordinating sites for heavy metal ions.<sup>162</sup> LMOF-263 exhibits remarkable water stability, a high BET surface area, and strong blue emission with an internal quantum yield of 89.2%. Notably, it detects toxic heavy metals in water even at extremely low con-

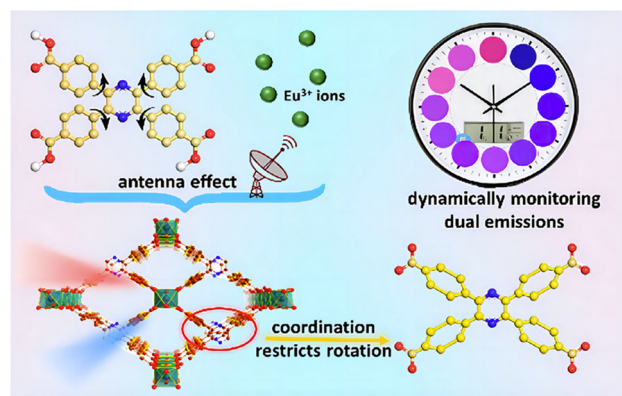


Fig. 10 Dual emission AIE-MOF for arginine detection. Adapted with permission from ref. 161 Copyright 2019, ACS.

centrations (19.7 ppb and 3.3 ppb for  $\text{Pb}^{2+}$  and  $\text{Hg}^{2+}$ , respectively) through a fluorescence quenching mechanism. Additionally, the incorporation of thio-functionalized sites enhances its preference for heavier metal ions compared to lighter ones. Similar to this, Zhang *et al.* developed a highly sensitive fluorescent probe by integrating 6-aza-2-thiothymine-stabilized gold nanoclusters (ATT-AuNCs), showing AIE behaviour, onto a cerium-based MOF *via* electrostatic interactions, forming the hybrid material AuNCs/Ce-MOF.<sup>163</sup> The enhanced fluorescence performance arises from the dual influence of the AIE-active nanoclusters and the structural rigidity of the MOF, which effectively limit molecular vibrations. Additionally, the Ce-MOF acts as a pre-concentration platform, selectively capturing  $\text{Hg}^{2+}$  ions near the fluorophores, and thereby improving the recognition efficiency. The composite sensor demonstrated a broad linear response range from 0.2 to 500  $\text{ng mL}^{-1}$  and an ultra-low limit of detection of 0.067  $\text{ng mL}^{-1}$  ( $\sim 0.33$  nM). Application testing in real world samples showed excellent agreement with standardized analytical methods. Hence, this presents an effective strategy to both intensify the fluorescence of nanoclusters and achieve the trace-level detection of heavy metal ions in complex environments, with significant promise for environmental monitoring.

Moreover, chemical sensors based on luminescence exhibit optical signal transduction through changes in luminescence wavelength or intensity. For example, here, typically, if the framework of the host molecular orbitals align well with the guest analytes, electron and/or energy transfer governs the phenomenon of signal transduction within the MOF. For example, in the case of the turn-off sensing of mycotoxins, a TPPE-based profoundly luminescent 3D Zn-MOF was developed by Li and colleagues.<sup>88</sup> This Zn-MOF is extremely porous and exhibits intense blue-green emission, showcasing an impressive internal quantum yield of 92.7%. Further, monitoring aflatoxins, among the most prevalent mycotoxins globally, is essential for ensuring food security and preventing crop contamination. The Zn-MOF demonstrates a rapid and highly sensitive reaction to aflatoxins through the mechanism of fluo-



rescence quenching. Notably, it achieves a limit of detection of 46 ppb for aflatoxin B1, the most toxic aflatoxin and highly potent natural carcinogen, positioning Zn-MOF amongst the most effective fluorescent chemosensors.

Photosensitizers (PSs) for photodynamic therapy (PDT) have attracted considerable attention owing to their capability to reduce nonspecific phototoxic damage, ultimately enhancing treatment consequences. Compared to traditional treatment approaches such as chemotherapy, radiotherapy, and surgery, PDT based on non-toxic PSs offers notable benefits, including the capability for real-time photoluminescence imaging for diagnostic purposes and reduced systemic toxicity.<sup>164</sup> AIE-MOFs can function as PSs to produce reactive oxygen species (ROS) *via* localized excitation, inducing cellular apoptosis and facilitating the ablation of tumor tissues. Additionally, their porous assembly enables efficient drug loading. Upon exposure to the acidic tumor microenvironment, the MOFs degrade, releasing the drugs in a targeted manner. These unique properties help minimize the damage to healthy cells, thus rendering AIE-MOFs attractive candidates for photodynamic and antibacterial therapies.

Research on PDT has shown that the interaction between copper nodes and glutathione (GSH) in AIE-MOFs can be boosted, enabling controlled PDT activation. This regulation reduces ROS loss in zebrafish and cancer cells, leading to amended therapeutic consequences. Expanding on these insights, Liu and colleagues established that a Cu-MOF, namely MOF-199 (Fig. 11A), with AIE activity can act like a stimuli-responsive material, minimizing the loss of ROS and enhancing PDT effectiveness.<sup>165</sup> To accomplish this, this group integrated an AIE-based activatable PS, specifically 2-(4-(diphenylamino)phenyl)anthracene-9,10-dione (TPAAQ), into MOF-199, creating TPAAQ@MOF-199 nanoparticles (Fig. 11B). These nanoparticles demonstrated efficient internalization by tumor cells. Upon photoactivation, endogenous GSH triggered the breakdown of the MOF-199 structure through coordination competition, releasing the encapsulated PSs based on AIE to produce ROS. Moreover, both *in vivo* and *in vitro* experiments confirmed that TPAAQ@MOF-199 effectively destroyed tumour cells, while exhibiting negligible phototoxicity to regular cells, demonstrating it as a promising candidate for antitumor PDT, as shown in Fig. 11D. Further, this strategy was extended to

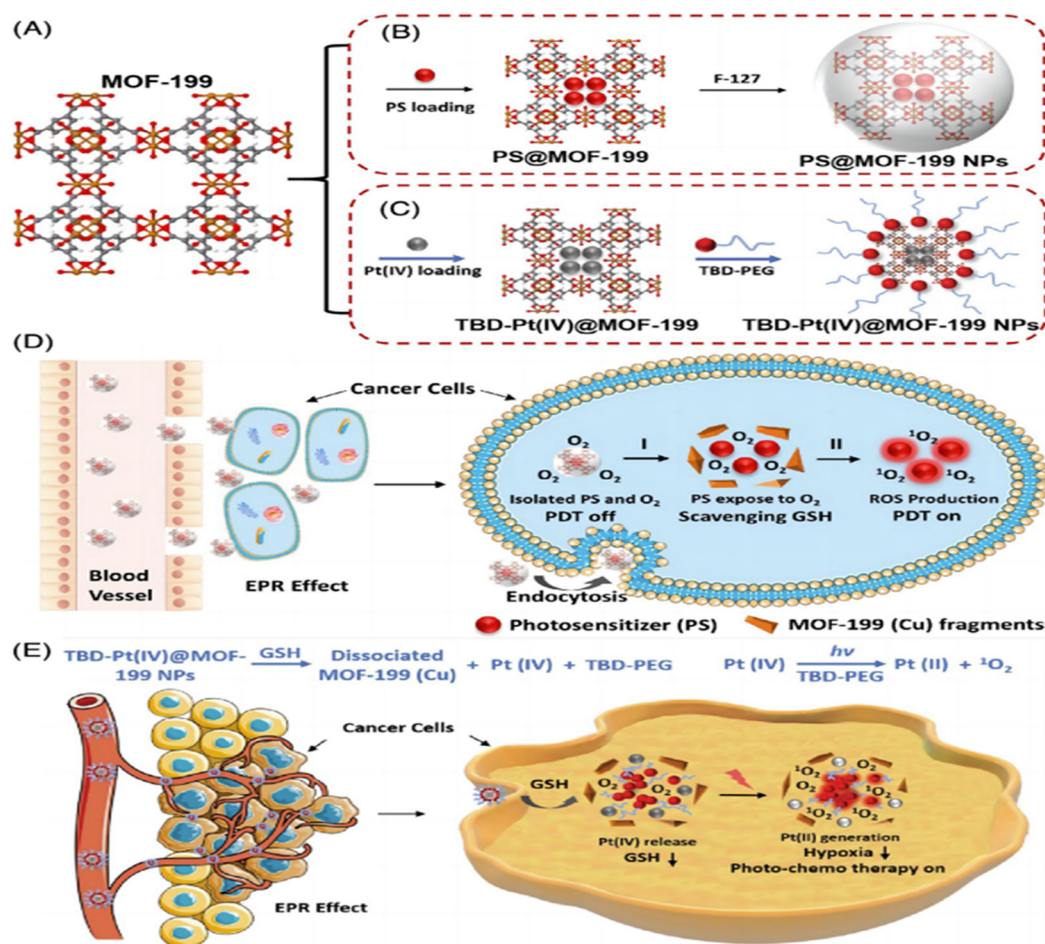


**Fig. 11** (A) Crystalline structure of MOF-199. Synthetic schemes for (B) TPAAQ@MOF-199 NPs and (C) TBD-Pt(IV)@MOF-199 NPs. Illustration of tumor treatment using (D) TPAAQ@MOF-199 NPs and (E) TBD-Pt(IV)@MOF-199 NPs. Adapted with permission from ref. 165 Copyright 2019, ACS.

PSs having both ACQ and AIE properties to develop activatable PDT along with image-guided features. Additionally, regulating the tumor microenvironment by reducing the levels of GSH and easing hypoxia, facilitates regulated chemo drug release and site-specific drug delivery. Liu and colleagues applied this concept by incorporating a diazido complex of platinum(IV) into MOF-199, creating Pt(IV)@MOF-199. They subsequently altered it with a tetraphenylethylene derivative (TBD), which is an AIE PS conjugated with polyethylene glycol, forming TBD-Pt(IV)@MOF-199 (Fig. 11C).<sup>166</sup> Once absorbed in tumor cells, TBD-Pt(IV)@MOF-199 effectively depleted the GSH present within the cells and degraded into smaller fragments, releasing Pt(IV). Under light irradiation, Pt(IV) generated O<sub>2</sub> to alleviate the tumor hypoxia, while converting into a Pt(II)-based chemotherapeutic drug inside the tumor cells. Additionally, TBD efficiently produced ROS and emitted sharp luminescence, facilitating combined chemotherapy as well as image-guided phototherapy (Fig. 11E). This innovative composite photomaterial based on AIE presents significant potential for enhancing antitumor therapy by combining photodynamic and chemotherapy approaches for optimal therapeutic efficacy.

Liu and colleagues introduced a straightforward and versatile approach for developing PSs by integrating MIL-100(Fe) with numerous AIE-based PSs.<sup>167</sup> The photosensitization efficiency of PSs encapsulated in the interior of MIL-100(Fe) was markedly improved owing to their initial separation from O<sub>2</sub>. The interaction of iron(III) within MIL-100(Fe) produced H<sub>2</sub>O<sub>2</sub>, which subsequently triggered the disintegration of the MOF structure. This breakdown exposed the embedded AIE PSs to O<sub>2</sub>, activating photosensitization. Additionally, the breakdown of H<sub>2</sub>O<sub>2</sub> further generated O<sub>2</sub>, helping to mitigate the tumor hypoxia and improve the effectiveness of PDT.

Furthermore, Liu and colleagues employed ZIF-8 as a carrier to encapsulate AIE PSs, leveraging its porous construction to enhance the diffusion of oxygen and boost <sup>1</sup>O<sub>2</sub> generation within tumors upon light exposure. The resulting PS@ZIF-8-PMMA-S-S-mPEG demonstrated self-assembling capability triggered by the intratumoral cleavage of its disulfide bonds. This auto-assembly promoted higher intertumoral ROS production and optimum tumor retention, thereby maximizing the PDT efficacy. Overall, this strategy provides a versatile approach for constructing PSs@MOFs, offering an efficient platform for enhanced PDT treatment.<sup>168</sup> The integration of drugs with AIE can also be utilized for antimicrobial therapy. Liu and colleagues introduced an innovative strategy by designing AIE-MOF-based nanocomposites for image-guided antimicrobial treatment and *in vivo* bacterial metabolic labelling (Fig. 12).<sup>169</sup> They encapsulated 3-azidod-alanine, *i.e.*, d-AzAla, a bacterial metabolism labelling species, in MIL-100(Fe) to synthesize d-AzAla@MIL-100 composites. The composites facilitated the site-specific release of d-AzAla at the infected sites through the disintegration of MIL-100(Fe). Once absorbed by bacteria, the azide groups of d-AzAla were incorporated into their cell wall. Subsequently, nano-sized AIE-based particles functionalized by dibenzocyclooctyne (DBCO) units were utilized to trace *Staphylococcus aureus* (MRSA) in contaminated dermal tissues. Upon light exposure, these nanocarriers effectively eliminated the pathogens and mitigated severe inflammatory responses. Additionally, Wang and colleagues verified that the excitation of localized surface plasmon resonance (LSPR) inside gold nanostars (AuNSs) substantially enhanced the antimicrobial efficacy of Zn-MOF nanosheets, further advancing the potential of MOF-based antimicrobial strategies.<sup>170</sup> The AuNSs/Zn-MOF nanosheets demonstrated a 2.5-

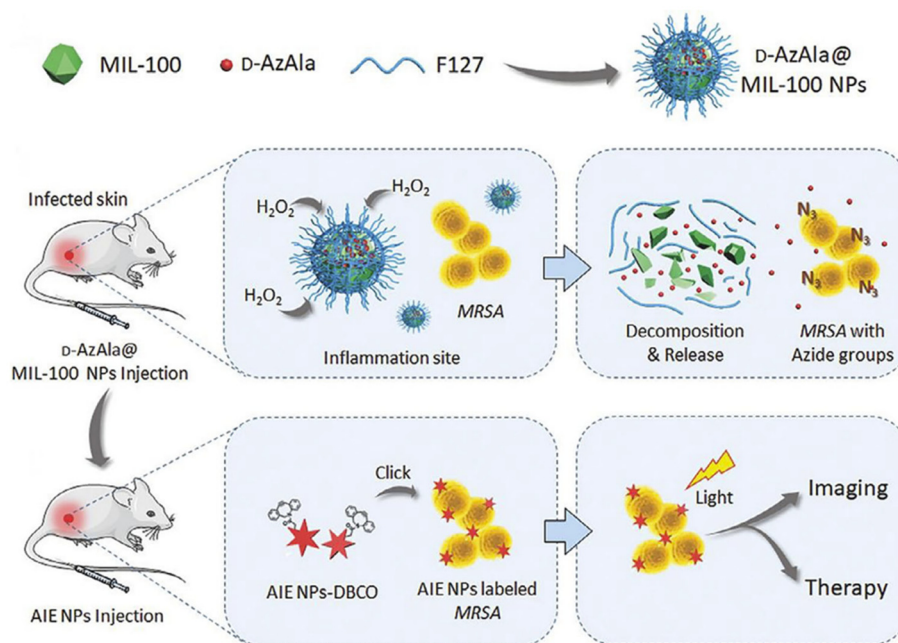


Fig. 12 Strategic illustration of antibacterial treatment utilising d-AzAla@MIL-100(Fe) NPs.<sup>169</sup>

fold increase in ROS production for bacterial inactivation under light irradiation. The mechanistic studies attributed this enhancement to a plasmon-induced “dual-excited synergistic effect”. Firstly, the photosensitive Zn-MOF nanosheets were directly excited to generate ROS with antibacterial properties. Additionally, the excitation of LSPR led to the formation of highly concentrated plasmonic hot electrons over the surface of AuNSs. These electrons were transferred to Zn-MOF from the AuNSs due to energy alignment, creating an electron-rich environment. This facilitated the activation of adsorbed O<sub>2</sub> molecules, promoting their breakdown into ROS for efficient microbial neutralization. This research underscores the potential of LSPR excitation in amplifying the antimicrobial efficacy of MOFs and introduces a new approach for advanced antibacterial treatment.

Building on these findings, AIE-based MOFs have emerged as promising photosensitizers as well as drug transporters, demonstrating great efficacy in disease treatment. However, to maximize their therapeutic potential, while minimizing side effects, several challenges must be addressed. Firstly, improving the photosensitivity and targeting capability of AIE-based MOFs is crucial to attain a high ROS concentration at the targeted site, ensuring optimal treatment outcomes. Secondly, a deeper understanding of their metabolic pathways within the body is necessary to minimize residual metal ions and organic ligands, thereby reducing the risk of subordinate toxicity. In conclusion, AIE-based MOFs hold great promise for therapeutic applications; however, additional investigations and advancements are needed in this direction to facilitate their broad medical applications.

### 3.2. Detection of volatile organic compounds

Volatile organic compounds (VOCs) comprise several airborne pollutants including ketones, xylene, toluene, styrene, benzene, chlorinated hydrocarbons, aldehydes, and ethylbenzene. Inhalation of these substances can trigger serious health risks. Furthermore, long-term contact with VOCs, even on the concentration scale of parts per million (ppm), may cause damage to the nervous and immune systems.<sup>171–173</sup> Consequently, developing efficient methods for VOC detection remains a critical area of research.

The luminescent recognition of guest moieties was achieved by enhancing *in situ* RIM through the guest-induced locking mechanism, as shown in Fig. 13A, where Lang and colleagues showcased the efficacy of a robust Cu(I)-MOF  $[\text{Cu}_4\text{I}_4(\text{Py}_3\text{P})_2]_n$ ,  $\text{Py}_3\text{P}$  = tris(2-pyridyl)phosphine). The Cu(I)-MOF features hexagonal pores capable of hosting guest moieties.<sup>174</sup> The luminescence emission strength of the Cu(I)-MOF increased markedly upon exposure to hydrocarbons that are chlorinated (Fig. 13B). Further, the single-crystal X-ray diffraction (SC-XRD) analysis demonstrated that the proximity between  $\text{CH}_2\text{Cl}_2/\text{CHCl}_3$  and the Cu(I)-MOF facilitated weak interactions, thereby effectively restricting its molecular vibrations, and thus enhancing its luminescence (Fig. 13C). In contrast, other gases exhibited either a longer distance or higher disorder in guest molecule arrangement, leading to weaker interactions, which failed to

lock molecular vibrations. Further, DFT calculations were performed to assess the impact of  $\text{CH}_2\text{Cl}_2$ ,  $\text{CHCl}_3$ , and  $\text{CCl}_4$  on the Cu(I)-MOF. The findings indicated that the void area of the MOF can entirely be employed by three molecules of  $\text{CHCl}_3$  or  $\text{CH}_2\text{Cl}_2$ , leading to improved luminescence. However, the incorporation of three  $\text{CCl}_4$  moieties was determined to be disadvantageous, preventing sufficient vibration sealing and resulting in weaker luminescence. This emission amplification due to guest confinement allows Cu(I)-MOF to selectively detect chlorinated hydrocarbons with an ultra-fast detection time of less than 0.6 seconds (Fig. 13D). Furthermore, an *on-off* demonstration with multiple cycles was shown for  $\text{CH}_2\text{Cl}_2$  successfully (Fig. 13E). Hence, this research presents an innovative guest-lock-induced activation strategy for the rapid luminescent sensing of guest moieties.

In a similar context for the sensing of chlorinated VOCs, Zhao and colleagues developed a copper(I)-cluster-based metal organic framework,  $[\text{Cu}_3\text{I}_3(\text{TPSA})\cdot\text{CH}_3\text{CN}]_n$ , by coordinating CuI with the AIE-capable ligand TPSA (*N,N',N''*-tri(3-pyridine)thiotriamide phosphate).<sup>175</sup> This MOF exhibits ligand-centered cyan luminescence at 485 nm upon excitation at 377 nm, with a decay lifetime of 5.2  $\mu\text{s}$ . Structural analysis revealed a 3D network with 1D channels and strong Cu...Cu cuprophilic interactions (2.547–2.780 Å). This framework demonstrates excellent water, acid-base (pH 2–13), solvent (THF, ethanol, DMF), and thermal stability up to  $\sim 200^\circ\text{C}$ . Remarkably, this material displays distinct luminescent responses towards chlorinated VOCs,  $\text{CH}_2\text{Cl}_2$ ,  $\text{CHCl}_3$ , and  $\text{CCl}_4$ , both in the solvent and vapor phases. Exposure to saturated  $\text{CH}_2\text{Cl}_2$  vapor results in a 274.2% luminescence enhancement, whereas  $\text{CHCl}_3$  causes 62.5% quenching, and  $\text{CCl}_4$  produces a negligible change. *In situ* gas sensing experiments showed a strong linear correlation between luminescence intensity and  $\text{CH}_2\text{Cl}_2$  vapor pressure, with a low detection limit of 0.4 Pa ( $\approx 3.7$  ppm), and a rapid response time of  $\sim 2$  s (visible to the naked eye under UV light), making it one of the fastest and most sensitive LMOF-based sensors reported to date. Similar turn-on/off responses were observed for 1,2-dichloroethane (LOD = 1.2 Pa and response time  $\approx 296$  s) and  $\text{CHCl}_3$  (LOD = 3.1 Pa and response time  $\approx 10$  s). The unique sensing mechanism is attributed to the manipulation of the weak host-guest and analyte interactions, which modulate the ligand vibration and non-radiative decay. Moreover, this MOF demonstrated excellent selectivity over other VOCs such as THF, DMF, acetone, methanol, ethanol, and toluene and showed outstanding stability and recyclability over 10 sensing cycles. Beyond sensing, the distinct turn-on/off emission behaviour was also employed for information encryption and logic gate operations, underscoring its multifunctionality and real-world applicability.

Liu, Zhao, and colleagues developed a porous 3D MOF featuring 1D channels TPE-MOF, namely,  $[\text{Zn}_2(\text{TCPPE})]_n$ .<sup>89</sup> Further, the MOF was activated by the solvent exchange method with  $\text{CH}_2\text{Cl}_2$ , and then isolated, which was named activated TPE-MOF. The fluorescence quantum yields of the activated and as-synthesized TPE-MOF were 11.3% and 7.2%,



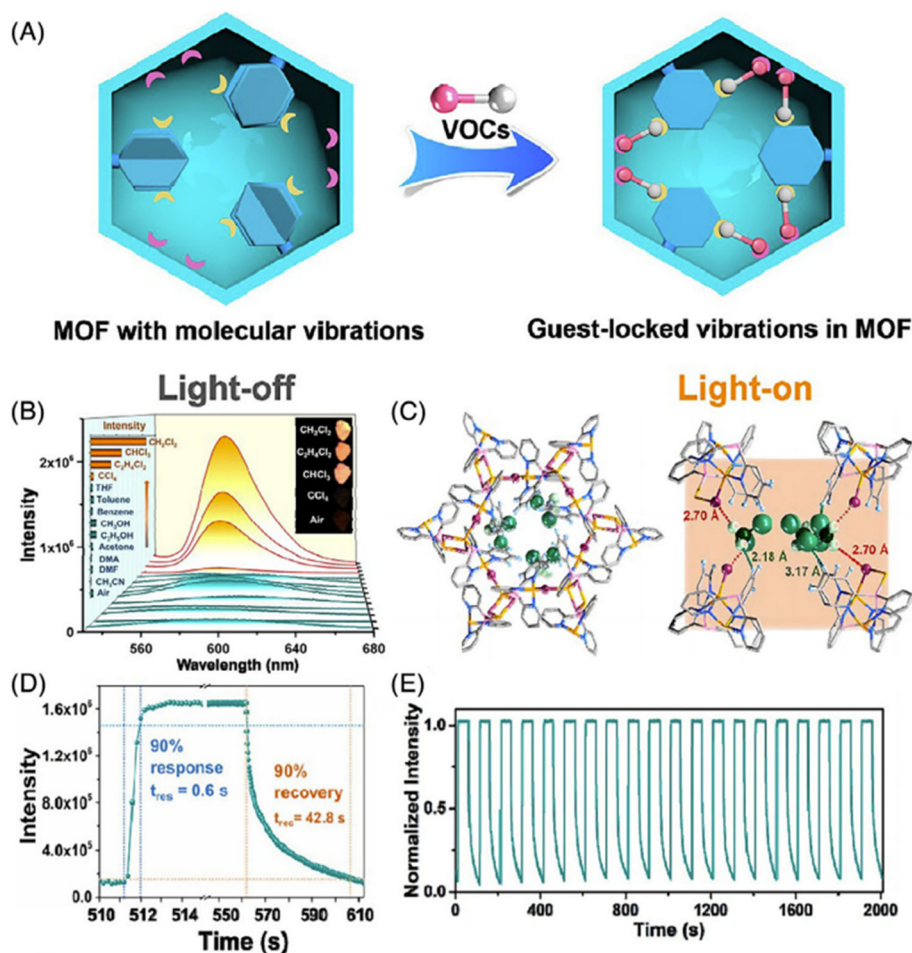


**Fig. 13** (A) Light-up luminescent sensing model by the guest-lock mechanism. (B) Cu(I)-MOF emission spectra when treated with guest moieties. (C) Assembly of  $\text{CH}_2\text{Cl}_2$ @Cu(I)-MOF. (D) Response spectrum of Cu(I)-MOF to  $\text{CH}_2\text{Cl}_2$ . (E) On-off luminescent detection. Adapted with permission from ref. 174 Copyright 2020, ACS.

respectively. Upon activation, the emission maximum of the TPE-MOF undergoes a significant red shift from 470 nm to 535 nm, whereas the presence of mesitylene, benzene, aliphatic VOCs or *m*-xylene induced a blue shift. This response to VOCs is likely due to the conformational changes in the phenyl rings of the TCPPE unit. Additionally, the fluorescence of the activated TPE-MOF is drastically quenched by nitroaromatics, which is attributed to an electron transfer effect, further demonstrating its potential for nitroaromatic detection.

Furthermore, Zhu and collaborators developed UiO-66-TBPE, UiO-66 modified with tetraphenylethylene (TBPE), which exhibits the representative blue emission of the TBPE linkers.<sup>176</sup> This MOF worked as a highly effective luminescent sensor for the rapid and preferential detection of styrene and *p*-xylene vapours, with detection limits of 0.906 and 1.295 ppm, respectively. Studies showed that the luminescence enhancement in the presence of *p*-xylene was primarily attributed to the robust interactions between the partial RIR of the phenyls of TBPE and *p*-xylene, along with presence of  $\pi$ - $\pi$

interactions amongst these aromatic rings. In contrast, styrene deactivated the luminescence of the UiO-66-TBPE, as shown by powder XRD and luminescence spectroscopy. These studies confirmed that the luminescence deactivation effect observed was not due to structural disintegration of FRET. Instead, DFT calculations indicated that UiO-66-TBPE has a higher excited LUMO energy level than styrene, allowing a charge transfer pathway upon 365 nm excitation. This suggests that the quenching was likely caused by photoinduced electron transfer (PET) from UiO-66-TBPE to styrene. To improve the real-world usability, UiO-66-TBPE was united with polyacrylate to form a versatile composite membrane, which displayed rapid styrene vapor recognition within just 30 s.

Moreover, Tang *et al.* demonstrated a fluorescence “turn-on” sensing approach for VOCs using TPE-based NUS-1 and NUS-1a (an activated form of the former) MOFs and 4,4'-(2,2-diphenylethene-1,1-diyl)dibenzoic acid (DPEB) as a linker.<sup>87</sup> The MOFs have a 2D sheet-like structure featuring broad hexagonal pores. A key structural feature of NUS-1 is that all the pendent phenyl rings align within the tunnels and retain

rotational freedom even after MOF assembly. This unique arrangement facilitates robust associations between the analytes and phenyl rings, restricting their movement, and thereby enabling a *turn-on* fluorescence emission. Moreover, the activated form of NUS-1, *i.e.*, NUS-1a, which is its dehydrated form (solvent molecules were evacuated), retains the same space group and structural integrity as NUS-1, indicating the stability of its structure and making it suitable for advanced chemical detection studies. However, the fluorescence quantum yield of NUS-1a is limited to 15%, which is significantly lower than that of the free TPE-based ligand (79%). This decrease is ascribed to the nonradiative exciton decay caused by the unrestricted vibration and rotation of the phenyl rings. Additionally, NUS-1a shows a marginally reduced quantum yield with a 19 nm bathochromic shift in its emission curve compared to NUS-1. VOC detection experiments revealed that NUS-1a exhibits a *turn-on* fluorescence effect for several analytes, including toluene, mesitylene, benzene and xylene. Among them, NUS-1a  $\supset$  benzene displayed the most pronounced red shift of 18 nm, whereas NUS-1a  $\supset$  mesitylene exhibited the most pronounced blue shift of 28 nm. Furthermore, the fluorescence quantum yield of the NUS-1a  $\supset$  benzene adduct reached an impressive value of 49% from 15%. These findings highlight that analyte-specific interactions with the pendent phenyl rings effectively hinder their motion, further reducing nonradiative exciton dissipation and enhancing the fluorescence, thereby making NUS-1a a promising material for VOC detection.

In addition, Wang and coworkers synthesized a 2D MOF based on TTPE,  $[\text{Mn}(\text{TTPE})\text{Cl}_2]_4\text{CHCl}_3)_n$ , by functionalizing the TPE core with triazole units. This material exhibits the capability for SC-SC (single crystal-to-single crystal) conversion, enabling its structural conversion into  $[\text{Mn}(\text{TTPE})(\text{H}_2\text{O})_2](\text{ClO}_4)_2 \cdot 0.5\text{TTPE} \cdot 5 \cdot 25\text{H}_2\text{O})_n$ , an additional 2D structure, upon encapsulating the bulky modified aromatic molecule 1,1,2,2-tetrakis[4-(1*H*-1,2,4-triazol-1-yl)phenyl]ethylene (TTPE). This transformation indicates the adaptability and tunability of the framework, making it a potential contender for guest-sensitive fluorescent materials. The ability of the framework to undergo precise modifications without losing its crystalline integrity suggests its potential applications in chemical sensing, selective adsorption, and fluorescence-based detection systems.<sup>177</sup> These two luminescent TTPE-based materials,  $[\text{Mn}(\text{TTPE})\text{Cl}_2]_4\text{CHCl}_3)_n$  and  $[\text{Mn}(\text{TTPE})(\text{H}_2\text{O})_2](\text{ClO}_4)_2 \cdot 0.5\text{TTPE} \cdot 5 \cdot 25\text{H}_2\text{O})_n$ , exhibit excellent selectivity for  $\text{Cd}^{2+}$  ions, making them promising candidates for heavy metal ion sensing. Additionally, the desolvated  $[\text{Mn}(\text{TTPE})(\text{H}_2\text{O})_2](\text{ClO}_4)_2 \cdot 0.5\text{TTPE} \cdot 5 \cdot 25\text{H}_2\text{O})_n$  undergoes a hypsochromic shift (blue shift in emission maximum) when exposed to various analytes, such as cyclohexanone, cyclohexanediol, cyclohexanediamine, and ethylenediamine, highlighting its potential in vapor-phase sensing applications. Similarly, other TPE-based MOFs, such as  $[\text{Cd}_2(\text{tpe})(\text{bpdc})_2(\text{H}_2\text{O})]^{178}$  and  $[\text{ZnCl}_2(\text{tpe})_4(\text{TCE})]^{179}$  exhibit intensified *turn-on* emission when exposed to benzene and its methyl-substituted analogues, demonstrating their ability to detect aromatic hydro-

carbons. Interestingly,  $[\text{ZnCl}_2(\text{tpe})_4(\text{TCE})]$  exhibits fluorescence quenching when interacting with nitro-phenyl-substituted VOCs, indicating its potential for the selective detection of nitroaromatic compounds, which are commonly associated with explosives and environmental pollutants. These findings reinforce the versatility of TTPE-based and TPE-based MOFs as highly selective luminescent sensors for metal ions, VOCs, and environmental pollutants. To provide a broader context for the sensing performance of AIE-MOFs, Table 1 presents a comparative overview of their key parameters such as detection limits (LOD) and response times. This compilation includes selected examples of both AIE-MOFs and conventional sensing materials, offering a survey of their performance characteristics across different VOC targets.

### 3.3. Nitroaromatics detection

In addition to the examples discussed in the previous section along with VOCs, here a few more cases of detecting and distinguishing energetic compounds such as TNP (2,4,6-trinitrophenol), DNP (2,4-dinitrophenol), TNT (2,4,6-trinitrotoluene), DNT (2,4-dinitrotoluene), 4-NP (4-nitrophenol), 2-NP (2-nitrophenol), *o*-DNB (1,2-dinitrobenzene), *p*-DNB (1,4-dinitrobenzene), *p*-NBA (4-nitrobenzoic acid), and NRHCs (nitrogen-rich heterocycles) is discussed given that they are crucial for environmental monitoring and national security.<sup>198,199</sup> However, their structural similarity poses a significant challenge for universal discrimination. As discussed previously, AIE-MOFs equipped with TPE have demonstrated significant potential in detecting these compounds owing to their greater selectivity, fluorescence turn-on/off mechanisms, and strong interactions with nitroaromatics. Researchers aim to design ultra-sensitive and selective sensing platforms for energetic complexes, ensuring rapid and accurate detection in security, environmental safety, and forensic applications.

For example, Luo and colleagues designed a fluorescent sensing array comprising eight AIE-MOFs, namely AM<sub>x</sub> (where *x* is from 1 to 7), based on TPPE or 1,2-diphenyl-1,2-bis(4-(pyridin-4-yl)-phenyl)ethene (ByTPE) as linkers and other co-ligands.<sup>200</sup> AM<sub>x</sub> was further specifically labelled based on the metal ion present in it and the type of linker and co-ligands used. These AM<sub>x</sub> enabled the differentiation of nine energetic compounds into three groups including nitrogen-rich heterocycles (NRHCs), nitroaromatics, and nitramines (Fig. 14A). The array exhibited a detection range of 300  $\mu\text{M}$  to 10 nM and demonstrated excellent selectivity against various competitive molecules (Fig. 14B). The extremely nitrated NACs (TNP, TNT, and LTNR) effectively deactivated the luminescence of nucleophilic AM<sub>x</sub>, which was supported by DFT calculations, showing their lower LUMO energy levels than AIE linkers (Fig. 14C). In contrast, NRHCs (DHT, NTO, DNBT, and DABT) exhibited distinct quenching behaviours due to variations in their structures and functional groups. Since DABT has a high LUMO energy level and lacks spectral overlap, it exhibited inefficient quenching of AM<sub>x</sub> luminescence. The luminescence response mechanisms were influenced by both the AM<sub>x</sub> topology and the properties of the energetic compounds. This mul-



**Table 1** Comparative performance of AIE-MOFs and conventional sensors in detecting volatile organic compounds (VOCs)

Material	Target VOC(s)	Response time	Limit of detection (LOD)	Sensitivity and selectivity remarks	Ref.
[Cu <sub>4</sub> I <sub>4</sub> (Py <sub>3</sub> P) <sub>2</sub> ] <sub>n</sub> (Cu(I)-MOF)	CH <sub>2</sub> Cl <sub>2</sub> , CHCl <sub>3</sub> , CCl <sub>4</sub>	<0.6 s	N/A	Guest-lock-induced turn-on; highly selective for chlorinated VOCs; $\Phi_{\text{FS}}$ enhanced upon analyte entry	174
[[Cu <sub>3</sub> I <sub>3</sub> (TPSA)]·CH <sub>3</sub> CN] <sub>n</sub>	CH <sub>2</sub> Cl <sub>2</sub> , CHCl <sub>3</sub> , CCl <sub>4</sub> , 1,2-dichloroethane	~2 s (CH <sub>2</sub> Cl <sub>2</sub> ), 10 s (CHCl <sub>3</sub> ), 296 s (DCE)	0.4 Pa (CH <sub>2</sub> Cl <sub>2</sub> ), 3.1 Pa (CHCl <sub>3</sub> ), 1.2 Pa (DCE)	274.2% turn-on for CH <sub>2</sub> Cl <sub>2</sub> ; 62.5% quenching for CHCl <sub>3</sub> ; high selectivity over other VOCs (e.g., THF, DMF, toluene)	175
UiO-66-TBPE	<i>p</i> -Xylene, styrene	~30 s (PA membrane)	1.295 ppm ( <i>p</i> -xylene), 0.906 ppm (styrene)	Turn-on for <i>p</i> -xylene; PET quenching for styrene	176
[Zn <sub>2</sub> (TCPPE)] (TPE-MOF)	Benzene, <i>m</i> -xylene, mesitylene, aliphatics	N/A	N/A	Emission shifts due to phenyl conformational pairing; $\Phi_{\text{FS}}$ : 7.2% (as-synthesized) → 11.3% (activated)	89
NUS-1a (TPE-MOF)	Mesitylene, xylene, toluene, benzene	N/A	N/A	Turn-on response and high quantum yield recovery; $\Phi_{\text{FS}}$ : 15% (free) → 49% (benzene-loaded)	87
AuPt@ZnO nanoflowers	Toluene (also benzene, toluene, and xylene mix)	22.4 s	0.5 ppm	High sensitivity (response 69.7 to 50 ppm); operation at 175 °C	180
Au-coated SnO <sub>2</sub> nanorods	Benzene, toluene, xylene, formaldehyde (BTXF)	≤2.5 s (10 ppm)	~10 ppb (formaldehyde)	Excellent indoor VOC detection with high response	181
MWCNT (multiwall carbon nanotube)	Acetone, ethanol, isopropanol and isoprene	110 s	9 ppm	Sensitivity: 0.0672	182
CNT (carbon nanotube)	Toluene, methanol, acetone, xylene, chloroform, benzene	125 s	5 ppm	Sensitivity: 0.62%	183
GO (graphene oxide)	Ethanol, acetone, and ethylbenzene	80–340 s	100 ppb	Sensitivity: 600 ppb	184
3DMxene	Acetone, methanol, and ethanol	<2 min	50 ppb	Sensing range: 50 ppb up to a saturated vapour	185
SnO <sub>2</sub>	Benzene, toluene, xylene vapours	Benzene: 238 s, toluene: 26 s, xylene: 35 s	Benzene: 2 ppm, Toluene: 1.5 ppm, Xylene: 0.2 ppm	Dynamic sensing range: 0.2–11 ppm	186
CuO/Cu <sub>2</sub> O	Acetone	122–205 s (depends on vapour concentration)	N/A	Sensing range: 0.125–1000 ppm	187
ZnO	Benzene, toluene, ethanol, and xylene	N/A	20 ppb	Sensing range: 1–9 ppm	188
ZrO <sub>2</sub>	Acetone, ethanol, H <sub>2</sub> O <sub>2</sub> , 2,4-DNT, 2,3-dimethyl-2,3-dinitrobutane (DMNB), ethylene glycol dinitrate (EGDN), nitroglycerine (NG)	10 s	N/A	The relative response to acetone is greater than that compared to Ethanol	189
390HUA zeolite	Acetone, ethanol, acetaldehyde, ammonia	3.6 s	N/A	Sensitivity: 3.47	190
HZSM-5 zeolite	Methanol, ethanol, acetone, and CO	N/A	0.5 ppm	Response value: 10 (for 100 ppm of CO)	191
ZSM-5 zeolite	Methanol, ethanol, acetone	26–65 s	0.4455 ppm	N/A	192
Zeolite Y (DaY)	Propanol, formaldehyde, and toluene	10 s (at 275 °C)	N/A	~96% response value for propanol	193
SiO <sub>2</sub>	Toluene, benzene, chloroform, and acetone	N/A	107.8 ppm for toluene	N/A	194
Silica	Ethanol, acetone, aromatic benzene, toluene, chlorobenzene	Benzene: 60–100 s, toluene: 115–140 s, acetone: 95–285 s	ppb level	Insensitive to nonpolar ethane or hexane	195
ZIF-8	Aldehydes	N/A	7.7 ppb	N/A	196
PDMS (polydimethylsiloxane)	Benzene, toluene, and xylene	<2 s	N/A	Sensitivity for benzene: 1601.3, toluene: 782.8, xylene: 289.1 ppm nm <sup>-1</sup>	197

ticomponent fluorescent array presents a more efficient strategy compared to sensors utilizing individual AIE-based MOFs for detecting structurally similar energetic compounds.

In another case, Wang and co-workers developed a Zr-based MOF functionalized with TPE units using a mixed-ligand approach, similar to the previous example, by incorporating

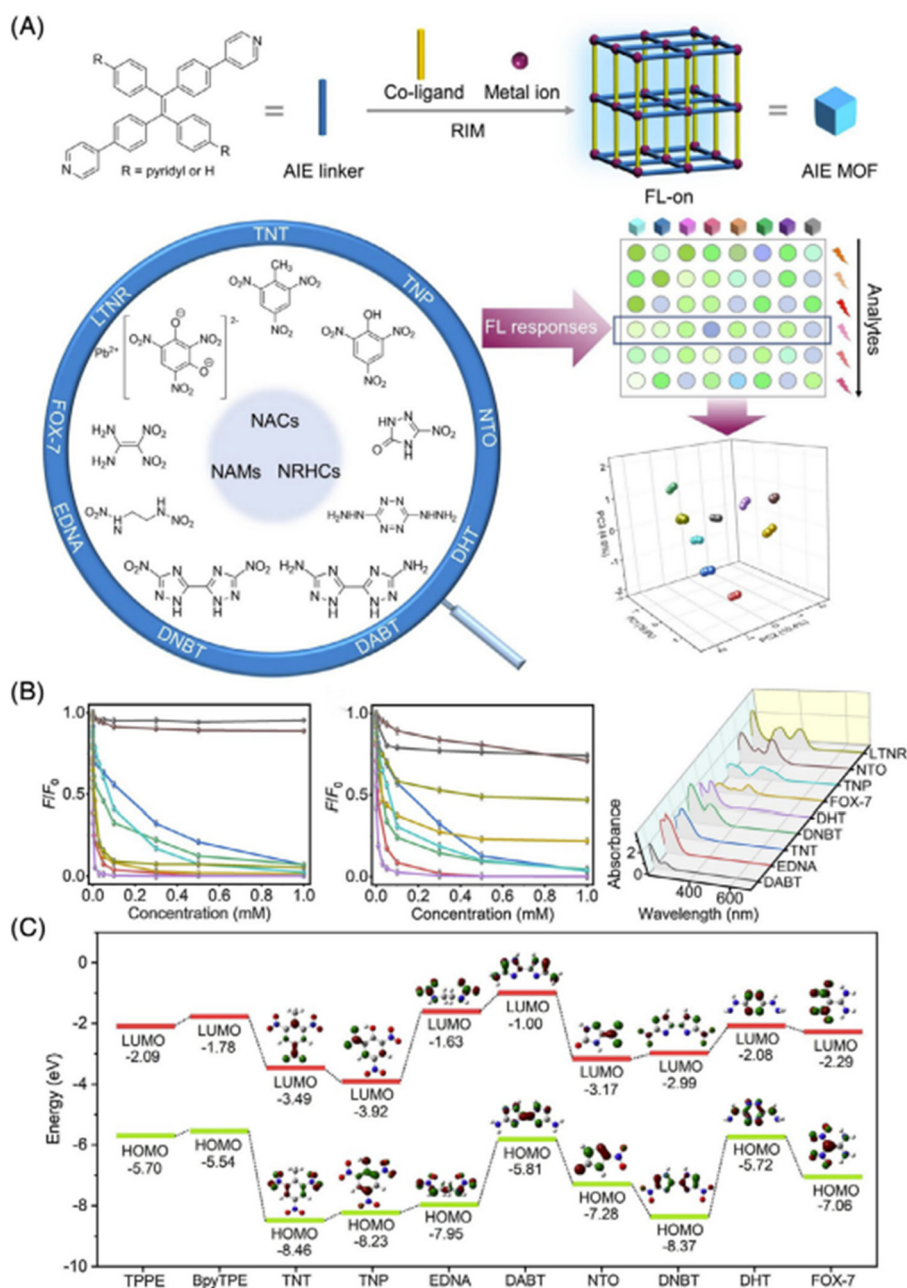


**Fig. 14** (A) Illustration of a multicomponent AIE-MOF sensing array for detecting energetic complexes. (B) Sensitivity and selectivity of AIE-MOFs. (C) Theoretical calculation of sensing mechanism. Adapted with permission from ref. 200 Copyright 2021, Elsevier.

$H_2$ -etpdc and  $H_2$ -mtpdc dicarboxylate struts.<sup>201</sup> This strategy enables the integration of the TPE unit, despite its significant steric obstruction, while preserving the porosity of the MOF for analyte diffusion. The resulting MOF exhibits blue-green fluorescence, having a quantum yield up to 48%. When exposed to nitroaromatic explosives, it undergoes preferential fluorescence suppression in the presence of TNP due to hydrogen-bonding and sturdy electrostatic interactions with the hydroxyl groups of nitrophenols and Lewis basic nitrogen donor sites of the imidazole ligand. This facilitates the transfer of energy and electrons from TPE to nitrophenols, *i.e.*, from

electron-rich units to electron-deficient units. Additionally, this MOF demonstrates highly effective catalytic performance in aerobic cross-dehydrogenative coupling reactions driven by visible light, whereas the comparable system of the UiO-68-mtpdc MOF, which lacked the TPE unit, shows no catalytic activity. This confirms the crucial role of the AIE-active TPE core as the active photocatalyst in Zr-MOF. Furthermore, Lin, Zhao, and co-workers synthesized two AIE fluorescent MOFs,  $Zn_2(H_2L)_2(Bpy)_2(H_2O)_3 \cdot H_2O$  and  $Zn_2(L)(H_2O)(DMA) \cdot DMA$ , using a TPE analogue, having a benzene core and modified with tetracarboxylate.<sup>202</sup> These MOFs exhibit absolute

quantum yields of 37% and 43%, respectively. Notably,  $\text{Zn}_2(\text{H}_2\text{L})_2(\text{Bpy})_2(\text{H}_2\text{O})_3 \cdot \text{H}_2\text{O}$  displays exceptional selectivity and sensitivity for TNP recognition in aqueous media, demonstrating superior fluorescence quenching compared to other nitro explosives.

In a similar context, Wang and co-workers utilized metal ions with different outer electron configurations and AIEgen linkers to develop various MOFs for the *turn-on* sensing of energetic heterocyclic complexes (EHCs).<sup>37</sup> This team synthesized three MOFs, namely, TABD-MOF-1, -2, and -3, by coordinating di-substituted TABDCOOH with  $\text{Mg}^{2+}$ ,  $\text{Ni}^{2+}$ , and  $\text{Co}^{2+}$ , respectively. These MOFs exhibited diverse fluorescence characteristics. TABD-MOF-1 showed extreme fluorescence; however, TABD-MOF-2 displayed minimal fluorescence, and TABD-MOF-3 was completely non-fluorescent due to the LMCT (ligand to metal charge transfer) phenomenon, with quantum yields of 38.5%, 1.12%, and 0.15%, respectively. Notably, the non-fluorescent cobalt-based TABD-MOF-3 demonstrated superior sensitivity and selectivity towards five-membered ring energetic nitrogen-based heterocycles (5MR-EHCs)-such as azoxyfurazans, tetrazoles, triazoles, and their derivatives, hybrids, and salts, which are typically undetectable by conventional fluorometric methods that rely on energy or electron transfer mechanisms. The  $\text{C}=\text{N}$  and  $\text{N}=\text{N}$  bonds in 5MR-EHCs enabled the dissociation of the metal-linker coordinate bond in TABD-MOFs through competitive coordination. This disruption of the metal-linker interactions interrupt the LMCT process, releasing the TABD linkers, which then accumulate to form extremely emissive moieties. In the case of 5-nitro-2,4-dihydro-3H-1,2,4-triazole-3-one (NTO) detection,

TABD-MOF-3 achieved an extremely low solid-state sensing limit of  $6.5 \text{ ng cm}^{-2}$  with a solution sensing limit of  $10^{-9} \text{ mol L}^{-1}$ , with signal transduction discernible to the bare eyes (Fig. 15).

Furthermore, Guan and colleagues reported the fabrication of a thorium-based metal organic framework, Th-TCBPE, synthesized *via* coordination between  $\text{Th}(\text{NO}_3)_4$  and an AIE-active ligand,  $\text{H}_4\text{TCBPE}$ .<sup>203</sup> The resulting structure is a highly stable, interpenetrated two-dimensional network featuring bicapped dodecahedral  $\text{ThO}_{10}$  nodes. This MOF exhibits typical aggregation-induced emission behaviour of weak luminescence in dilute THF solutions, which becomes significantly enhanced upon increasing the proportion of THF or adjusting the water/THF ratios, confirming its AIE nature. Notably, Th-TCBPE functions as a sensitive and selective fluorescent sensor for various NACs, such as nitrophenol, nitrotoluene, and dinitrotoluene. The fluorescence quenching mechanism is ascribed to photoinduced electron transfer from the electron-rich TCBPE ligand to the electron-deficient NACs. This material demonstrates detection limits in the low micromolar range of approximately  $1\text{--}2 \text{ }\mu\text{M}$  for compounds such as TNP and DNT, along with a rapid fluorescence quenching response within 30 s, and excellent selectivity over non-nitro analogues. This research represents a pioneering application of thorium-based MOFs incorporating TPE-derived linkers for efficient NAC sensing, combining robust structural features with practical sensing functionality. To contextualize this advancement, Table 2 provides a comparative overview of AIE-MOF-based and conventional sensing systems used for nitroaromatic compound detection, highlighting their key performance para-

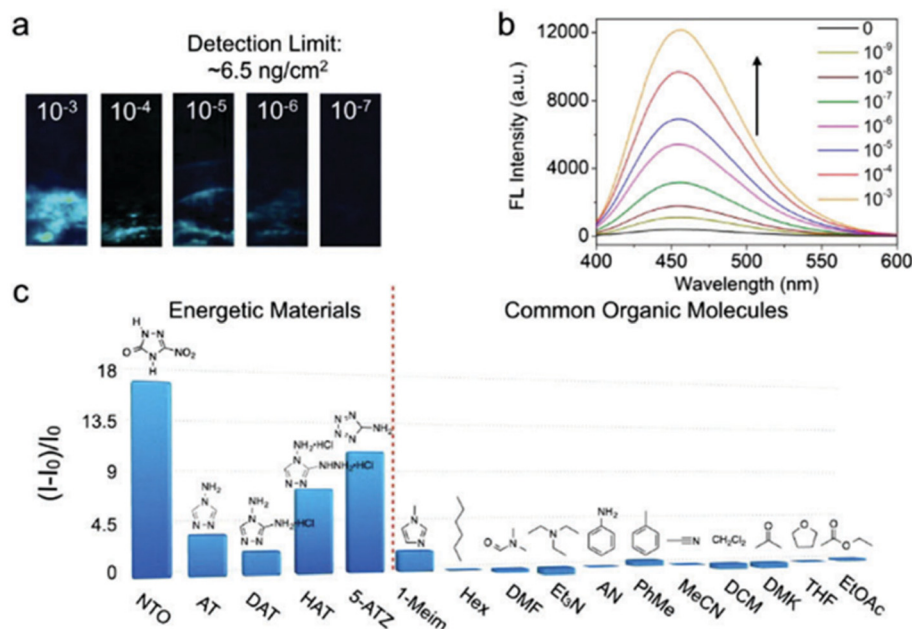


**Fig. 15** (a) Images of paper strips coated with TABD-MOF-3 after adding various concentrations of NTO in THF solution, observed under UV light. (b) Fluorescence spectra of TABD-MOF-3 in THF after the addition of NTO solution at varying concentrations, followed by the introduction of hexane. (c) Efficiency of fluorescence enhancement  $((I - I_0)/I_0)$  measured for various analytes using TABD-MOF-3 at an excitation wavelength of 360 nm. Adapted with permission from ref. 37 Copyright 2021, Elsevier.

**Table 2** Performance comparison of AIE-MOFs and conventional sensors for nitroaromatic detection

Materials	Target NAC(s)	Limit of detection (LOD)	Response time	Sensitivity and selectivity remarks	Ref.
Zr-MOF (TPE-MOF)	TNP, DNP	N/A	N/A	Selective quenching <i>via</i> imidazole-nitrophenol interactions; $\Phi_{\text{FL}} \approx 48\%$	201
$[\text{Zn}_2(\text{H}_2\text{L})_2(\text{Bpy})_2(\text{H}_2\text{O})_3 \cdot \text{H}_2\text{O}]$	TNP	N/A	N/A	$\Phi_{\text{FL}} \approx 37\%$ in aqueous phase, quenched by TNP	202
$[\text{Zn}_2(\text{L})(\text{H}_2\text{O})(\text{DMA}) \cdot \text{DMA}]$	TNP	$\sim 110$ ppb (0.49 mM)	N/A	$\Phi_{\text{FL}} \approx 43\%$ ; high water-phase sensitivity	202
TABD-MOF-1 (Mg-MOF)	NTD	N/A	N/A	Highly fluorescent baseline; provides “turn-on” potential upon analyte exposure	37
TABD-MOF-2 (Ni-MOF)	NTD	N/A	N/A	Minimal fluorescence improves selectivity relative to Mg/Co analogues	37
TABD-MOF-3 (Co-MOF)	NTD	$10^{-9}$ M (solution), $6.5 \text{ ng cm}^{-2}$	N/A	Turn-on emission <i>via</i> LMCT suppression; selective for 5-membered heterocycles	37
Th-TCBPE	TNP, DNP, 4-NP, 2-NP, <i>o</i> -DNB, <i>p</i> -DNB, <i>p</i> -NBA	TNP: $0.47 \mu\text{M}$ DNP: $0.40 \mu\text{M}$ 4-NP: $0.70 \mu\text{M}$ 2-NP: $0.44 \mu\text{M}$ <i>o</i> -DNB: $0.71 \mu\text{M}$ <i>p</i> -DNB: $0.91 \mu\text{M}$ <i>p</i> -NBA: $1.55 \mu\text{M}$	N/A	Low $\mu\text{M}$ sensitivity ( $1\text{--}2 \mu\text{M}$ ); strong selectivity over non-nitro aromatics; rapid quenching ( $\sim 30$ s)	203
Graphene/graphite MIP (molecularly imprinted polymer) nanocomposite	Nitro-benzene vapours	0.2 ppm	N/A	N/A	204
MIP thin film@ZnO nanorods	4-NP	$0.036 \mu\text{M}$	9 min	Sensitivity: $K_{\text{SV}} \sim 197\,440 \text{ M}^{-1}$	205
MIP-capped CdTe quantum dots	4-NP	$0.040 \mu\text{M}$	12 min	Sensitivity: $K_{\text{SV}} \sim 33\,500 \text{ M}^{-1}$	206
Fluorescent-labeled imprinted polymer	DNT, TNT	DNT: $30.1 \mu\text{M}$ TNT: $40.7 \mu\text{M}$	$\sim 1$ min	N/A	207
MIP/ZnO-MWCNTs-CTS(chitosan)/ITO (indium-tin oxide) sensor	4-NP	$0.001 \mu\text{M}$	N/A	Sensitivity: $53.219 \mu\text{A (cm}^2 \text{ mM)}^{-1}$	208
MIP-CP(carbon paste) voltammetric sensor	4-NP	$0.003 \mu\text{M}$	$\sim 10$ min	N/A	209
Photocathode-based PFC (photocatalytic fuel cell)	4-NP	$0.031 \mu\text{M}$	$\sim 20$ s	Sensitivity: $0.0295 \text{ V}^1$	210
MIP@thiophene thin film	DNT	Piezoelectric Micro-gravimetry (PM): $0.76 \text{ mM}$	10 min	N/A	211
Pyrene-based supramolecular polymers	TNP, TNT	ppt level	Rapid (not timed)	Acids (carboxylic groups) exhibited greater sensitivity than corresponding esters	212

meters such as detection limit, sensitivity, response time, and selectivity.

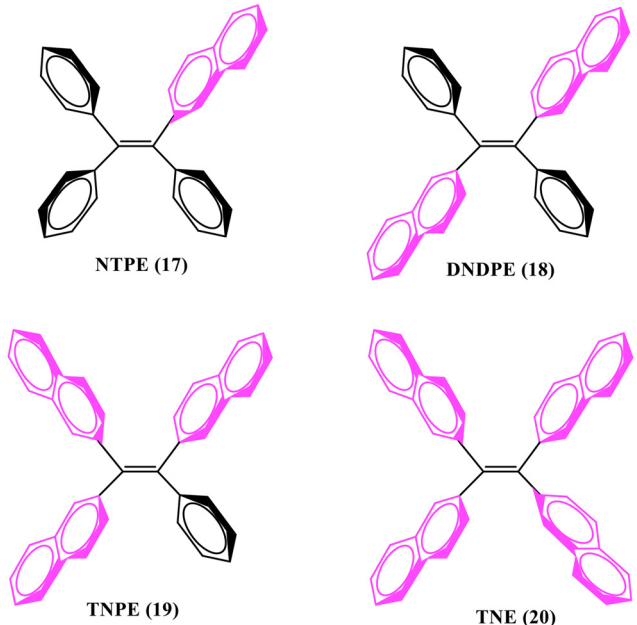
### 3.4. Development of luminescent materials responsive to external stimuli

Stimuli-responsive luminescent compounds possess exceptional properties that allow them to alter their photo-fluorescence emission upon exposure to external factors such as pressure, light, temperature, pH, and specific species. Their ability to dynamically adjust their fluorescence intensity or wavelength makes them highly suitable for sensing and detection applications. These materials are widely explored for use in environmental monitoring, biomedical diagnostics, and security screening. By leveraging their tunable optical properties, researchers are continuously developing innovative solutions for real-time and highly sensitive detection systems. For example, Shi and co-workers developed two innovative porous MOFs based on tetraphenylethylene (TPE) named Sr-ETTB and Co-ETTB.<sup>213</sup> In these MOFs, by altering their outer

shell electron configurations from  $\text{Sr}^{2+}$  to  $\text{Co}^{2+}$  ions, this team successfully tuned their fluorescence properties from intense emission in the former to total quenching in the later. Sr-ETTB exhibited efficient blue luminescence with reversible responses to pressure and temperature variations, covering sensing ranges of 1 atm to 12.38 GPa and 80 to 400 K, respectively. The resulting luminescence modulation clearly correlated with structural deformations within the crystal lattice. Conversely, Co-ETTB, initially non-emissive, displayed turn-on luminescence during interaction with histidine, triggered by the liberation of the AIE linker *via* competitive coordination replacement, thereby activating its AIE properties. This study offers a straightforward strategy for designing luminescent materials responsive to external stimuli with diverse applications in the environment, distinguishing and biochemical detection.

Furthermore, a highly delicate detection technique is essential to detect organophosphorus pesticides (OPs) given that they suppress acetylcholinesterase activity, leading to neuro-



**Table 3** Substitution of TPE phenyl rings with naphthalene to synthesize new AIEgens


	$\lambda_{\text{abs}}/\text{nm}$	$\lambda_{\text{abs}}/\text{nm}$		$\phi_{\text{F}} (\%)$		$\alpha_{\text{AIE}}^e$
	Soln	Soln <sup>a</sup>	Film <sup>b</sup>	Soln <sup>c</sup>	Film <sup>d</sup>	
TPE	299	—	475	0.24	49.2	205
NTPE	324	392	487	0.81	45.0	56
DNDPE	333	393	491	1.09	30.1	28
TNPE	341	393	493	1.64	37.4	23
TNE	349	394	494	1.66	22.4	13

<sup>a</sup> In THF solvent (10  $\mu\text{M}$ ). <sup>b</sup> Thin film deposited on a quartz substrate. <sup>c</sup> Measured in THF solvent with 9,10-diphenylanthracene ( $\phi_{\text{F}} = 90\%$  in cyclohexane) as the reference standard. <sup>d</sup> Measured in an amorphous film using an integrating sphere. <sup>e</sup>  $\alpha_{\text{AIE}} = \phi_{\text{F,A}}/\phi_{\text{F,S}}$ .

logical disorders. In this context, Liu and colleagues designed AIE-active AuNCs@ZIF-8, which has efficient fluorescence emission with an excited-state lifetime of 6.83  $\mu\text{s}$  and quantum yield of 4.63%.<sup>214</sup> Here, this team developed a dual-signal biosensor by integrating fluorescence and colorimetric signals based on the enzymatic reaction of choline oxidase and acetylcholinesterase with AuNCs@ZIF-8. The luminescent MOF was easily decapsulated to release AuNCs, and further ZIF-8 also decomposed in the presence of oxidants such as  $\text{H}_2\text{O}_2$ , causing the fluorescence to turn off. The  $\text{H}_2\text{O}_2$  is produced *in situ* by the enzymatic reaction of acetylcholinesterase (AChE), followed by choline oxidase. Simultaneously, the produced AuNCs acted as mimics of peroxidase and catalyzed the oxidation of 3,3',5,5'-tetramethylbenzidine, thereby generating a distinct blue color. Conversely, the addition of OPs inhibits the AChE activity, thereby turning on the fluorescence. Thus, this fluorescence-colorimetric biosensor worked based on stimulus response to the presence/absence of  $\text{H}_2\text{O}_2$ , thereby monitoring the amounts of OPs in the solution or solid state. Additionally, colorimetric strips of paper were produced for

easy pictorial, semi-quantitative sensing, whereas a smart-phone application was introduced to enhance the visualization accuracy and enable real-time pesticide contamination monitoring, making this system both accessible and efficient.

Further, Dincă and colleagues developed AIE-MOFs for the specific sensing of ammonia at high temperatures.<sup>86</sup> In this study, a TPE-based  $\text{Zn}_2(\text{TCPE})$  MOF was utilized, which retained its intense luminescence up to 350  $^\circ\text{C}$ , which is just below its degradation temperature of 400  $^\circ\text{C}$ . Additionally, it maintained its emission strength and structural order over three consecutive heating-cooling cycles, whereas TPE alone exhibited significant fluorescence quenching when heated. This remarkable thermal stability in the  $\text{Zn}_2(\text{TCPE})$  MOF was attributed to its rigid structure, which effectively restricted vibrational energy dissipation. When the activated Zn-MOF was exposed to triethylamine, ammonia, water vapor, ethylenediamine, and *N,N*-diethylformamide, and at room temperature, only minimal changes in its emission maximum were observed for all analytes. However, at 100  $^\circ\text{C}$ , the  $\text{Zn}_2(\text{TCPE})$  MOF displayed exceptional selectivity for ammonia, as evidenced by the significant red-shift in emission maximum from 487 to 511 nm, whereas no effect was observed with the other analytes. This unique specificity was ascribed to the high affinity interaction between  $\text{Zn}^{2+}$  and  $\text{NH}_3$  ions, as confirmed by DFT calculations, highlighting the potential of  $\text{Zn}_2(\text{TCPE})$  as a robust high-temperature ammonia sensor.

Moreover, Zhang and co-authors designed an innovative guest@MOF composite, embedding TPE into the pores of the zeolitic imidazolate framework ZIF-71, creating what is referred to as TPE@ZIF-71.<sup>215</sup> Under ambient conditions, the fluorescence of TPE@ZIF-71 is weak due to the inherent phenyl ring motion of TPE. However, upon applying hydrostatic pressure *via* pellet formation, the framework constrains the molecular motion of TPE. *In situ* terahertz vibrational spectroscopy revealed enhanced nanoconfinement effects, increasing the vibrational restrictions, which turn on the fluorescence. Remarkably, the pressure-induced emission enhancement is reversible, and the composite retains its luminescence even after the stress is released, a clear “recording” of stress history. Quantitatively, compared to bare crystalline TPE, the pressure sensitivity is improved by more than 10-fold due to the MOF nanoconfinement. The emission intensity shows a monotonic increase with pressure, even at relatively low applied stress levels (<350 MPa in the pellet). Structural studies using X-ray diffraction and synchrotron far-infrared spectroscopy confirmed partial compression and framework amorphization, which lift the volumetric confinement restrictions on the guest motion. Critically, the rigid structure of ZIF-71 prevents TPE from recrystallizing once the pressure is released, enabling this material to “remember” the maximum pressure applied. This is notable for its potential in stress-sensing applications, given that it allows cumulative stress tracking, which conventional mechanofluorochromic systems cannot achieve.

Liu and colleagues, in their work, synthesized two novel lead-based AIE-MOFs, namely  $[\text{Pb}_2(\text{ETTC})(\text{DMA})_2] \cdot 2\text{DMA}$  (1)



and  $[(\text{CH}_3)_2\text{NH}_2] \cdot [\text{Pb}_2\text{Na}(\text{HETTC})_2] \cdot 5.5\text{DMA}$  (2), by incorporating the tetra-carboxylate AIE ligand  $\text{H}_4\text{ETTC}$  (ethene-1,1,2,2-tetrarlaytetrabenzoic acid).<sup>216</sup> Both MOFs adopt three-dimensional architectures, featuring one-dimensional channels, with compound 2 also incorporating sodium ions, which modulate its photophysical behaviour. Remarkably, unlike conventional luminescent systems that exhibit fluorescence quenching upon heating, these materials displayed an uncommon fluorescence turn-on response with an increase in temperature. Across the measured temperature range of 10 to 300 K, the fluorescence intensity of both frameworks progressively increased, with compound 2 exhibiting a more pronounced ratiometric response. This thermally activated emission behaviour was attributed to the restriction of intramolecular motions (RIM) within the framework. Specifically, the  $\text{Na}^+$ -containing MOF (2) presented a more distinct and stable emission shift, making it more suitable for temperature sensing. This study highlights the potential of AIE-based MOFs as ratiometric luminescent thermometers, offering excellent sensitivity, structural stability, and a clear linear correlation between temperature and emission intensity, which are particularly valuable for low-temperature photonic applications.

In a similar context, Chen Wang and co-workers developed a fluorescent Cd-tcbpe MOF with the molecular formula  $[\text{Cd}_3(\text{tcbpe})_{1.5}(\text{DMF})(\text{H}_2\text{O})_2] \cdot 6 \text{ DMF}$ , using the tetraphenylethene-derived tetracarboxylic acid ligand  $\text{H}_4\text{tcbpe}$ .<sup>217</sup> This material crystallizes into a three-dimensional porous structure and exhibits an initial cyan fluorescence emission centered at 475 nm, with a notable photoluminescence quantum yield of 64.3%. This MOF demonstrated remarkable multi-stimuli responsiveness to external conditions such as mechanical stress, humidity, solvent vapor, and temperature. Upon mechanical grinding, the emission red-shifted significantly from 475 nm to approximately 535 nm, with the fluorescence lifetime extending from 1.45 to 2.52 nanoseconds and quantum yield increasing to 125.6%, attributed to the intensified restriction of intramolecular motions (RIM). This material also displayed pronounced hydrochromic behaviour, wherein exposure to relative humidity above 40% triggered a reversible emission shift to 517 nm due to the exchange of coordinated DMF molecules with water and subsequent compression of the framework. Similarly, exposure to acidic and basic vapors such as HCl,  $\text{NH}_3$ ,  $\text{CH}_3\text{COOH}$ , and  $\text{CF}_3\text{COOH}$  resulted in evident solvatochromic responses, causing further guest-induced compression and color shifts in the emission spectra. Moreover, the framework retained its structural integrity upon thermal treatment, as confirmed by PXRD and IR studies, while also exhibiting reversible thermochromic behaviour as the fluorescence changed in response to increasing temperature. These properties enabled the development of rewritable luminescent displays, where patterns such as letters could be mechanically imprinted on paper and polymer matrices, and subsequently erased by mild solvent exposure, marking the applicability of the MOF in pressure sensing, anti-counterfeiting, and visual memory storage. The integration of high fluorescence efficiency, structural robustness, and multi-mode

stimuli responsiveness makes Cd-tcbpe a compelling example of advanced, multifunctional AIE-MOF design.

Furthermore, Rui Wang and co-workers engineered a magnetically recoverable MOF composite,  $\text{Fe}_3\text{O}_4@\text{ZW-MOF}$ , by growing a zwitterionic pyridinyl ligand-based MOF directly on  $\text{Fe}_3\text{O}_4$  nanoparticle cores (210 nm  $\rightarrow$  280 nm post-MOF) *via* a solvothermal process.<sup>218</sup> This composite exhibits reversible dual responsiveness to pH and visible/UV light, making it effective for the selective capture and release of phosphorylated peptides. Under visible-light irradiation, the pyridinyl-ZW ligands undergo photoinduced radical formation, generating positive charge gradients (zeta potential increases to +6.2 mV compared to +3.4 mV under UV). This enhanced positive surface charge promotes electrostatic attraction to negatively charged phosphorylated peptides, enabling efficient adsorption. Conversely, UV light reverses this charge gradient by reducing radicals, neutralizing the surface charge and facilitating peptide release. Thus, light stimulus acts as a switch for reversible capture/release cycles. Acidifying the medium protonates the pyridinium groups, further increasing the zeta potential (up to +26.7 mV under Vis/ $\text{H}^+$ ), and optimizing peptide capture. Under basic conditions, the surface charge flips to -46.3 mV under UV/ $\text{OH}^-$ , promoting efficient peptide desorption. Hence, pH tuning complements light control for precise peptide manipulation. Apart from this, the composite exhibited excellent performance metrics across several key parameters. It demonstrated remarkable sensitivity with a detection limit as low as 1 fmol for  $\beta$ -casein tryptic digests, successfully identifying three distinct phosphopeptides with high signal clarity. In terms of selectivity, this material showed impressive enrichment capabilities, effectively isolating phosphorylated peptides from  $\beta$ -casein/BSA mixtures even at a challenging 1 : 1000 mass ratio. This system also proved highly reusable, maintaining a consistent capture and release performance over 7 successive operational cycles without noticeable degradation. Furthermore, its versatility was evidenced through successful application to complex biological samples, where it enabled the isolation of 12 phosphopeptides from non-fat milk and 4 from human serum, highlighting its strong potential for real-world biochemical analysis.

## 4. Conclusion and our perspectives

This review provides a comprehensive overview of aggregation-caused quenching (ACQ) and aggregation-induced emission (AIE), while tracing historical development. Moreover, the luminescence pathways have been classified based on molecular structures, and the restriction of intramolecular rotation (RIR), intramolecular vibration (RIV), and intramolecular motion (RIM) mechanisms further discussed. Indeed, it was important to highlight how molecular rigidity and environmental factors influence emission properties. Furthermore, the key emphasis of this review study has been the strategic transformation of ACQ-active fluorophores (ACQphores) into AIE-active luminogens (AIEgens). Several approaches have

been explored in detail, including decorating ACQphores with AIEgens, partially replacing ACQphore segments with AIE-active units, designing new AIEgens derived from ACQphores, and incorporating triphenylamine (TPA) units to enhance the AIE characteristics. These methodologies have expanded the scope of luminescent materials, enabling the development of highly efficient fluorophores with improved optical properties and broader application potential. Furthermore, this review has delved into the emergence of AIE-based metal organic frameworks (AIE-MOFs) and their evolution in the field of luminescent sensing. By integrating AIEgens into MOF architectures, researchers have successfully developed materials with enhanced sensitivity, selectivity, and stability for detecting various analytes. Particular attention has been given to biological sensing, volatile organic compound (VOC) detection, heterocyclic compound identification, and nitroaromatic sensing. Additionally, the development of stimuli-responsive luminescent materials has been explored, emphasizing the ability of these robust materials to respond to environmental factors such as temperature, pressure, and pH. In conclusion, the study of AIE, ACQ, and their interconversion has paved the way for the rational design of advanced luminescent materials, with AIE-MOFs standing out as a unique class due to their ability to combine the structural tunability of MOFs with the solid-state emissive behaviour of AIEgens. Their intrinsic resistance to aggregation-caused quenching, high porosity, and capacity for post-synthetic functionalization endow them with exceptional advantages for selective, sensitive, and multi-mode sensing. Looking forward, AIE-MOFs hold immense potential for integration into wearable or portable diagnostic devices, enabling the real-time monitoring of environmental or biological analytes. Their adaptability makes them ideal for developing dual- or multi-signal sensing systems, such as fluorescence–colorimetric or fluorescence–electrochemical hybrids, improving both the detection accuracy and versatility. Further, their chemical robustness, emission tunability, and reusability make them attractive for on-site sensing in harsh or variable environments. A promising frontier lies in the application of machine learning and data-driven strategies to predict AIE-MOF behaviour, optimize sensor design, and accelerate material discovery. With continued innovation in ligand design, framework engineering, and device integration, AIE-MOFs are poised to become key enablers of next-generation smart sensing technologies.

## Author contributions

K. R. meticulously researched and crafted the comprehensive draft. Additionally, A. N. and R. J. provided guidance as a mentor, offering their expertise and granting final approval for the manuscript's final version.

## Conflicts of interest

There are no conflicts to declare.

## Data availability

No primary research results, software or code has been included and no new data were generated or analysed as part of this review.

## Acknowledgements

K. R. is thankful to the SVNIT, Surat, for providing a fellowship for her research work.

## References

- 1 M. D. E. Forbes, *ACS Cent. Sci.*, 2015, **1**, 354–363.
- 2 A. S. Manna, S. Ghosh, T. Ghosh, N. Karchaudhuri, S. Das, A. Roy and D. K. Maiti, *Chem. – Asian J.*, 2025, **20**, e202401328.
- 3 Y. Okada, M. Sugai and K. Chiba, *J. Org. Chem.*, 2016, **81**, 10922–10929.
- 4 S. W. Thomas, G. D. Joly and T. M. Swager, *Chem. Rev.*, 2007, **107**, 1339–1386.
- 5 F. J. M. Hoeben, P. Jonkheijm, E. W. Meijer and A. P. H. J. Schenning, *Chem. Rev.*, 2005, **105**, 1491–1546.
- 6 U. H. F. Bunz, *Chem. Rev.*, 2000, **100**, 1605–1644.
- 7 F. Hide, M. A. Díaz-García, B. J. Schwartz and A. J. Heeger, *Acc. Chem. Res.*, 1997, **30**, 430–436.
- 8 S. M. Borisov and O. S. Wolfbeis, *Chem. Rev.*, 2008, **108**, 423–461.
- 9 Y. Hong, J. W. Y. Lam and B. Z. Tang, *Chem. Soc. Rev.*, 2011, **40**, 5361–5388.
- 10 J. B. Birks, *Photophysics of aromatic molecules*, Wiley-Interscience, 1970.
- 11 L. Ma, X. Feng, S. Wang and B. Wang, *Mater. Chem. Front.*, 2017, **1**, 2474–2486.
- 12 J. Luo, Z. Xie, J. W. Y. Lam, L. Cheng, H. Chen, C. Qiu, H. S. Kwok, X. Zhan, Y. Liu, D. Zhu and B. Z. Tang, *Chem. Commun.*, 2001, 1740–1741.
- 13 Y. Hong, J. W. Y. Lam and B. Z. Tang, *Chem. Commun.*, 2009, 4332–4353.
- 14 J. Mei, N. L. C. Leung, R. T. K. Kwok, J. W. Y. Lam and B. Z. Tang, *Chem. Rev.*, 2015, **115**, 11718–11940.
- 15 J. Mei, Y. Hong, J. W. Y. Lam, A. Qin, Y. Tang and B. Z. Tang, *Adv. Mater.*, 2014, **26**, 5429–5479.
- 16 D. Ding, K. Li, B. Liu and B. Z. Tang, *Acc. Chem. Res.*, 2013, **46**, 2441–2453.
- 17 M. Wang, G. Zhang, D. Zhang, D. Zhu and B. Z. Tang, *J. Mater. Chem.*, 2010, **20**, 1858–1867.
- 18 Z. Chi, X. Zhang, B. Xu, X. Zhou, C. Ma, Y. Zhang, S. Liu and J. Xu, *Chem. Soc. Rev.*, 2012, **41**, 3878–3896.
- 19 Z. Zhao, J. W. Y. Lam and B. Z. Tang, *J. Mater. Chem.*, 2012, **22**, 23726–23740.
- 20 R. Hu, N. L. C. Leung and B. Z. Tang, *Chem. Soc. Rev.*, 2014, **43**, 4494–4562.

- 21 R. T. K. Kwok, C. W. T. Leung, J. W. Y. Lam and B. Z. Tang, *Chem. Soc. Rev.*, 2015, **44**, 4228–4238.
- 22 J. Chen, B. Xu, X. Ouyang, B. Z. Tang and Y. Cao, *J. Phys. Chem. A*, 2004, **108**, 7522–7526.
- 23 H. Tong, Y. Hong, Y. Dong, Y. Ren, M. Häussler, J. W. Y. Lam, K. S. Wong and B. Z. Tang, *J. Phys. Chem. B*, 2007, **111**, 2000–2007.
- 24 H. Tong, Y. Dong, Y. Hong, M. Häussler, J. W. Y. Lam, H. H. Y. Sung, X. Yu, J. Sun, I. D. Williams, H. S. Kwok and B. Z. Tang, *J. Phys. Chem. C*, 2007, **111**, 2287–2294.
- 25 Q. Zeng, Z. Li, Y. Dong, C. a. Di, A. Qin, Y. Hong, L. Ji, Z. Zhu, C. K. W. Jim, G. Yu, Q. Li, Z. Li, Y. Liu, J. Qin and B. Z. Tang, *Chem. Commun.*, 2007, 70–72.
- 26 Y. Dong, J. W. Y. Lam, A. Qin, J. Liu, Z. Li, B. Z. Tang, J. Sun and H. S. Kwok, *Appl. Phys. Lett.*, 2007, **91**, 011111.
- 27 F. Michael, *Chem. Eng. News Arch.*, 2001, **79**, 29–32.
- 28 T. Förster and K. Kasper, *Z. Phys. Chem.*, 1954, **1**, 275–277.
- 29 J. Liu, J. W. Lam and B. Z. Tang, *J. Inorg. Organomet. Polym. Mater.*, 2009, **19**, 249–285.
- 30 Y. Liu, C. Deng, L. Tang, A. Qin, R. Hu, J. Z. Sun and B. Z. Tang, *J. Am. Chem. Soc.*, 2011, **133**, 660–663.
- 31 Y. Hong, L. Meng, S. Chen, C. W. T. Leung, L.-T. Da, M. Faisal, D.-A. Silva, J. Liu, J. W. Y. Lam, X. Huang and B. Z. Tang, *J. Am. Chem. Soc.*, 2012, **134**, 1680–1689.
- 32 C. Zhang, S. Jin, K. Yang, X. Xue, Z. Li, Y. Jiang, W.-Q. Chen, L. Dai, G. Zou and X.-J. Liang, *ACS Appl. Mater. Interfaces*, 2014, **6**, 8971–8975.
- 33 N. Zhao, M. Li, Y. Yan, J. W. Y. Lam, Y. L. Zhang, Y. S. Zhao, K. S. Wong and B. Z. Tang, *J. Mater. Chem. C*, 2013, **1**, 4640–4646.
- 34 J. Chen and B. Tang, in *Restricted intramolecular rotations: a mechanism for aggregation-induced emission*, Wiley, New York, 2013, pp. 307–322.
- 35 D. Ding, C. C. Goh, G. Feng, Z. Zhao, J. Liu, R. Liu, N. Tomczak, J. Geng, B. Z. Tang, L. G. Ng and B. Liu, *Adv. Mater.*, 2013, **25**, 6083–6088.
- 36 E. Zhao, Y. Hong, S. Chen, C. W. T. Leung, C. Y. K. Chan, R. T. K. Kwok, J. W. Y. Lam and B. Z. Tang, *Adv. Healthcare Mater.*, 2014, **3**, 88–96.
- 37 Y. Guo, X. Feng, T. Han, S. Wang, Z. Lin, Y. Dong and B. Wang, *J. Am. Chem. Soc.*, 2014, **136**, 15485–15488.
- 38 N. Zhao, J. W. Y. Lam, H. H. Y. Sung, H. M. Su, I. D. Williams, K. S. Wong and B. Z. Tang, *Chem. – Eur. J.*, 2014, **20**, 133–138.
- 39 S. Asthana, M. S. S. V. Mouli, A. Tamrakar, M. A. Wani, A. K. Mishra, R. Pandey and M. D. Pandey, *Anal. Methods*, 2024, **16**, 4431–4484.
- 40 M. H. Chua, B. Y. K. Hui, K. L. O. Chin, Q. Zhu, X. Liu and J. Xu, *Mater. Chem. Front.*, 2023, **7**, 5561–5660.
- 41 Y. Li, L. Xu and B. Su, *Chem. Commun.*, 2012, **48**, 4109–4111.
- 42 Z. Jianyu, Z. Xueqian, S. Hanchen, W. Y. L. Jacky, Z. Haoke and B. Z. Tang, *Adv. Photonics*, 2021, **4**, 014001.
- 43 Y. Fang, K. Xu, D. He, W. Sun and W. Xiong, *Dyes Pigm.*, 2025, **235**, 112594.
- 44 Q. Li and Z. Li, *Adv. Sci.*, 2017, **4**, 1600484.
- 45 H. Wang, B. Aydiner, Z. Seferoglu, F. Bureš and J. Liu, *Dyes Pigm.*, 2022, **205**, 110354.
- 46 G. Jiang, J. Liu and P. Zhou, *J. Phys. Chem. A*, 2023, **127**, 5193–5201.
- 47 J. Liu, H. Su, L. Meng, Y. Zhao, C. Deng, J. C. Y. Ng, P. Lu, M. Faisal, J. W. Y. Lam, X. Huang, H. Wu, K. S. Wong and B. Z. Tang, *Chem. Sci.*, 2012, **3**, 2737–2747.
- 48 D. Zhao, F. Fan, J. Cheng, Y. Zhang, K. S. Wong, V. G. Chigrinov, H. S. Kwok, L. Guo and B. Z. Tang, *Adv. Opt. Mater.*, 2015, **3**, 199–202.
- 49 M. Wang, D. Zhang, G. Zhang and D. Zhu, *Chem. Phys. Lett.*, 2009, **475**, 64–67.
- 50 C. Y. Y. Yu, R. T. K. Kwok, J. Mei, Y. Hong, S. Chen, J. W. Y. Lam and B. Z. Tang, *Chem. Commun.*, 2014, **50**, 8134–8136.
- 51 P. Alam, M. Karanam, D. Bandyopadhyay, A. R. Choudhury and I. R. Laskar, *Eur. J. Inorg. Chem.*, 2014, **2014**, 3710–3719.
- 52 W. Zhou, Y. Tang, X. Zhang, S. Zhang, H. Xue and H. Pang, *Coord. Chem. Rev.*, 2023, **477**, 214949.
- 53 D. Dong, X. Zhao, C. Pu, Y. Yao, B. Zhao, G. Tian, G. Chang and X. Yang, *Inorg. Chem.*, 2023, **62**, 20528–20536.
- 54 X. Xu, T. Zhou, Y. Bing, X. Wang, H. Jiang, Z. Song and T. Zhang, *Adv. Funct. Mater.*, 2025, **35**, 2414141.
- 55 M. Pander, R. Gil-San-Millan, P. Delgado, C. Perona-Bermejo, U. Kostrzewa, K. Kaczkowski, D. J. Kubicki, J. A. R. Navarro and W. Bury, *Mater. Horiz.*, 2023, **10**, 1301–1308.
- 56 P.-H. Tong, J.-J. Wang, X.-L. Hu, T. D. James and X.-P. He, *Chem. Sci.*, 2023, **14**, 7762–7769.
- 57 N. Hussain and S. M. Mobin, *Chem. Sci.*, 2025, **16**, 8460–8469.
- 58 S. Ran, K. Sun, M. Zhao, Z. Wang, A. S. Alshammari, M. H. Helal, Z. M. El-Bahy, Y. Yuan and R. Fan, *Adv. Compos. Hybrid Mater.*, 2025, **8**, 1–32.
- 59 W. Chen, Y. Tan, H. Zheng, Z. Wang, Z. Qu and C. Wu, *Microchem. J.*, 2024, **206**, 111441.
- 60 X. Han, J. Li, S. Tao, G. Dou, S. Mansur and X. Zhang, *Molecules*, 2023, **28**, 5021.
- 61 T. Le Huec, A. López-Francés, I. A. Lázaro, S. Navalón, H. G. Baldoví and M. Giménez-Marqués, *ACS Nano*, 2024, **18**, 20201–20212.
- 62 M. D. Allendorf, C. A. Bauer, R. K. Bhakta and R. J. T. Houk, *Chem. Soc. Rev.*, 2009, **38**, 1330–1352.
- 63 Y. Cui, Y. Yue, G. Qian and B. Chen, *Chem. Rev.*, 2012, **112**, 1126–1162.
- 64 L. E. Kreno, K. Leong, O. K. Farha, M. Allendorf, R. P. Van Duyne and J. T. Hupp, *Chem. Rev.*, 2012, **112**, 1105–1125.
- 65 Z. Hu, B. J. Deibert and J. Li, *Chem. Soc. Rev.*, 2014, **43**, 5815–5840.
- 66 O. M. Yaghi, M. O’Keeffe, N. W. Ockwig, H. K. Chae, M. Eddaoudi and J. Kim, *Nature*, 2003, **423**, 705–714.
- 67 H.-C. Zhou, J. R. Long and O. M. Yaghi, *Chem. Rev.*, 2012, **112**, 673–674.
- 68 H. Furukawa, K. E. Cordova, M. O’Keeffe and O. M. Yaghi, *Science*, 2013, **341**, 1230444.

- 69 S. Qiu, M. Xue and G. Zhu, *Chem. Soc. Rev.*, 2014, **43**, 6116–6140.
- 70 A. G. Slater and A. I. Cooper, *Science*, 2015, **348**, aaa8075.
- 71 Y. Bai, Y. Dou, L.-H. Xie, W. Rutledge, J.-R. Li and H.-C. Zhou, *Chem. Soc. Rev.*, 2016, **45**, 2327–2367.
- 72 L. Wang, Y. Han, X. Feng, J. Zhou, P. Qi and B. Wang, *Coord. Chem. Rev.*, 2016, **307**, 361–381.
- 73 A. Schoedel, M. Li, D. Li, M. O'Keeffe and O. M. Yaghi, *Chem. Rev.*, 2016, **116**, 12466–12535.
- 74 J. Li, M. Xi, L. Hu, H. Sun, C. Zhu and W. Gu, *Anal. Chem.*, 2024, **96**, 2100–2106.
- 75 Y. Cheng, X. Yin, Y. Li, S. Wang, S. Xue, Q. Wu, J. Wang and D. Zhang, *Biosens. Bioelectron.*, 2024, **262**, 116556.
- 76 N. Wang, C. Wei, F. Wei, H. Huang, F. Huang, D. Chen, C. Yan and Y. Zhu, *J. Mater. Chem. A*, 2025, **13**, 13230–13247.
- 77 K. Song, X. Bi, C. Yu, Y.-T. Pan, P. Xiao, J. Wang, J.-I. Song, J. He and R. Yang, *ACS Appl. Mater. Interfaces*, 2024, **16**, 15227–15241.
- 78 N. B. Shustova, B. D. McCarthy and M. Dincă, *J. Am. Chem. Soc.*, 2011, **133**, 20126–20129.
- 79 N. B. Shustova, A. F. Cozzolino and M. Dincă, *J. Am. Chem. Soc.*, 2012, **134**, 19596–19599.
- 80 N. B. Shustova, T.-C. Ong, A. F. Cozzolino, V. K. Michaelis, R. G. Griffin and M. Dincă, *J. Am. Chem. Soc.*, 2012, **134**, 15061–15070.
- 81 Q. Gong, Z. Hu, B. J. Deibert, T. J. Emge, S. J. Teat, D. Banerjee, B. Mussman, N. D. Rudd and J. Li, *J. Am. Chem. Soc.*, 2014, **136**, 16724–16727.
- 82 Z. Wei, Z.-Y. Gu, R. K. Arvapally, Y.-P. Chen, R. N. McDougald Jr., J. F. Ivy, A. A. Yakovenko, D. Feng, M. A. Omary and H.-C. Zhou, *J. Am. Chem. Soc.*, 2014, **136**, 8269–8276.
- 83 Q. Zhang, J. Su, D. Feng, Z. Wei, X. Zou and H.-C. Zhou, *J. Am. Chem. Soc.*, 2015, **137**, 10064–10067.
- 84 Z. Hu, G. Huang, W. P. Lustig, F. Wang, H. Wang, S. J. Teat, D. Banerjee, D. Zhang and J. Li, *Chem. Commun.*, 2015, **51**, 3045–3048.
- 85 B. J. Deibert, E. Velasco, W. Liu, S. J. Teat, W. P. Lustig and J. Li, *Cryst. Growth Des.*, 2016, **16**, 4178–4182.
- 86 N. B. Shustova, A. F. Cozzolino, S. Reineke, M. Baldo and M. Dincă, *J. Am. Chem. Soc.*, 2013, **135**, 13326–13329.
- 87 M. Zhang, G. Feng, Z. Song, Y.-P. Zhou, H.-Y. Chao, D. Yuan, T. T. Y. Tan, Z. Guo, Z. Hu, B. Z. Tang, B. Liu and D. Zhao, *J. Am. Chem. Soc.*, 2014, **136**, 7241–7244.
- 88 Z. Hu, W. P. Lustig, J. Zhang, C. Zheng, H. Wang, S. J. Teat, Q. Gong, N. D. Rudd and J. Li, *J. Am. Chem. Soc.*, 2015, **137**, 16209–16215.
- 89 X.-G. Liu, H. Wang, B. Chen, Y. Zou, Z.-G. Gu, Z. Zhao and L. Shen, *Chem. Commun.*, 2015, **51**, 1677–1680.
- 90 Q. Xia, Y. Zhang, Y. Li, Y. Li, Y. Li, Z. Feng, X. Fan, J. Qian and H. Lin, *Aggregate*, 2022, **3**, e152.
- 91 H. Wang, E. Zhao, J. W. Y. Lam and B. Z. Tang, *Mater. Today*, 2015, **18**, 365–377.
- 92 Y. Tu, Z. Zhao, J. W. Y. Lam and B. Z. Tang, *Natl. Sci. Rev.*, 2021, **8**, nwaa260.
- 93 Q. Peng and Z. Shuai, *Aggregate*, 2021, **2**, e91.
- 94 Y. Y. Liu, X. Zhang, K. Li, Q. C. Peng, Y. J. Qin, H. W. Hou, S. Q. Zang and B. Z. Tang, *Angew. Chem., Int. Ed.*, 2021, **60**, 22417–22423.
- 95 J. Chen, C. C. W. Law, J. W. Y. Lam, Y. Dong, S. M. F. Lo, I. D. Williams, D. Zhu and B. Z. Tang, *Chem. Mater.*, 2003, **15**, 1535–1546.
- 96 X. Fan, J. Sun, F. Wang, Z. Chu, P. Wang, Y. Dong, R. Hu, B. Z. Tang and D. Zou, *Chem. Commun.*, 2008, 2989–2991.
- 97 S. Li, Q. Wang, Y. Qian, S. Wang, Y. Li and G. Yang, *J. Phys. Chem. A*, 2007, **111**, 11793–11800.
- 98 Q. Peng, Y. Yi, Z. Shuai and J. Shao, *J. Am. Chem. Soc.*, 2007, **129**, 9333–9339.
- 99 N. L. C. Leung, N. Xie, W. Yuan, Y. Liu, Q. Wu, Q. Peng, Q. Miao, J. W. Y. Lam and B. Z. Tang, *Chem. – Eur. J.*, 2014, **20**, 15349–15353.
- 100 Q. Zhu, L. Huang, Z. Chen, S. Zheng, L. Lv, Z. Zhu, D. Cao, H. Jiang and S. Liu, *Chem. – Eur. J.*, 2013, **19**, 1268–1280.
- 101 Y. Gong, Y. Tan, H. Li, Y. Zhang, W. Yuan, Y. Zhang, J. Sun and B. Z. Tang, *Sci. China: Chem.*, 2013, **56**, 1183–1186.
- 102 J. Luo, K. Song, F. I. Gu and Q. Miao, *Chem. Sci.*, 2011, **2**, 2029–2034.
- 103 L. Yao, S. Zhang, R. Wang, W. Li, F. Shen, B. Yang and Y. Ma, *Angew. Chem., Int. Ed.*, 2014, **53**, 2119–2123.
- 104 J. Liu, Q. Meng, X. Zhang, X. Lu, P. He, L. Jiang, H. Dong and W. Hu, *Chem. Commun.*, 2013, **49**, 1199–1201.
- 105 K. S. nee Kamaldeep, S. Kaur, V. Bhalla, M. Kumar and A. Gupta, *J. Mater. Chem. A*, 2014, **2**, 8369–8375.
- 106 J. L. Banal, J. M. White, K. P. Ghiggino and W. W. Wong, *Sci. Rep.*, 2014, **4**, 4635.
- 107 Z. Zhelev, H. Ohba and R. Bakalova, *J. Am. Chem. Soc.*, 2006, **128**, 6324–6325.
- 108 R. Bakalova, Z. Zhelev, I. Aoki, H. Ohba, Y. Imai and I. Kanno, *Anal. Chem.*, 2006, **78**, 5925–5932.
- 109 R. B. Thompson, *Fluorescence Sensors and Biosensors CRC Press*, 1st edn., 2005.
- 110 C. W. Tang and S. A. VanSlyke, *Appl. Phys. Lett.*, 1987, **51**, 913–915.
- 111 C. D. Geddes and J. R. Lakowicz, *Topics in Fluorescence Spectroscopy: Advanced Concepts in Fluorescence Sensing Part A: Small Molecule Sensing*, Springer, 2005.
- 112 E. A. Jares-Erijman and T. M. Jovin, *Nat. Biotechnol.*, 2003, **21**, 1387–1395.
- 113 H. Saigusa and E. Lim, *J. Phys. Chem.*, 1995, **99**, 15738–15747.
- 114 J. Wang, Y. Zhao, C. Dou, H. Sun, P. Xu, K. Ye, J. Zhang, S. Jiang, F. Li and Y. Wang, *J. Phys. Chem. B*, 2007, **111**, 5082–5089.
- 115 S. Hecht and J. M. J. Fréchet, *Angew. Chem., Int. Ed.*, 2001, **40**, 74–91.
- 116 B. T. Nguyen, J. E. Gautrot, C. Ji, P.-L. Brunner, M. T. Nguyen and X. X. Zhu, *Langmuir*, 2006, **22**, 4799–4803.
- 117 L. Chen, S. Xu, D. McBranch and D. Whitten, *J. Am. Chem. Soc.*, 2000, **122**, 9302–9303.



- 118 P. N. Taylor, M. J. O'Connell, L. A. McNeill, M. J. Hall, R. T. Aplin and H. L. Anderson, *Angew. Chem., Int. Ed.*, 2000, **39**, 3456–3460.
- 119 W. Z. Yuan, P. Lu, S. Chen, J. W. Lam, Z. Wang, Y. Liu, H. S. Kwok, Y. Ma and B. Z. Tang, *Adv. Mater.*, 2010, **22**, 2159–2163.
- 120 Y. Liu, S. Chen, J. W. Y. Lam, P. Lu, R. T. K. Kwok, F. Mahtab, H. S. Kwok and B. Z. Tang, *Chem. Mater.*, 2011, **23**, 2536–2544.
- 121 W. Z. Yuan, Y. Gong, S. Chen, X. Y. Shen, J. W. Y. Lam, P. Lu, Y. Lu, Z. Wang, R. Hu, N. Xie, H. S. Kwok, Y. Zhang, J. Z. Sun and B. Z. Tang, *Chem. Mater.*, 2012, **24**, 1518–1528.
- 122 W.-L. Gong, B. Wang, M. P. Aldred, C. Li, G.-F. Zhang, T. Chen, L. Wang and M.-Q. Zhu, *J. Mater. Chem. C*, 2014, **2**, 7001–7012.
- 123 W. Z. Yuan, Y. Tan, Y. Gong, P. Lu, J. W. Lam, X. Y. Shen, C. Feng, H. H. Y. Sung, Y. Lu and I. D. Williams, *Adv. Mater.*, 2013, **25**, 2837–2843.
- 124 Z. Zhao, P. Lu, J. W. Y. Lam, Z. Wang, C. Y. K. Chan, H. H. Y. Sung, I. D. Williams, Y. Ma and B. Z. Tang, *Chem. Sci.*, 2011, **2**, 672–675.
- 125 J. Huang, X. Yang, J. Wang, C. Zhong, L. Wang, J. Qin and Z. Li, *J. Mater. Chem.*, 2012, **22**, 2478–2484.
- 126 B. Xu, Z. Chi, Z. Yang, J. Chen, S. Deng, H. Li, X. Li, Y. Zhang, N. Xu and J. Xu, *J. Mater. Chem.*, 2010, **20**, 4135–4141.
- 127 Z. Zhao, B. Chen, J. Geng, Z. Chang, L. Aparicio-Ixta, H. Nie, C. C. Goh, L. G. Ng, A. Qin, G. Ramos-Ortiz, B. Liu and B. Z. Tang, *Part. Part. Syst. Character.*, 2014, **31**, 481–491.
- 128 Z. Zhao, C. Y. K. Chan, S. Chen, C. Deng, J. W. Y. Lam, C. K. W. Jim, Y. Hong, P. Lu, Z. Chang, X. Chen, P. Lu, H. S. Kwok, H. Qiu and B. Z. Tang, *J. Mater. Chem.*, 2012, **22**, 4527–4534.
- 129 W. Qin, J. Liu, S. Chen, J. W. Y. Lam, M. Arseneault, Z. Yang, Q. Zhao, H. S. Kwok and B. Z. Tang, *J. Mater. Chem. C*, 2014, **2**, 3756–3761.
- 130 X. Zhang, Z. Chi, B. Xu, H. Li, Z. Yang, X. Li, S. Liu, Y. Zhang and J. Xu, *Dyes Pigm.*, 2011, **89**, 56–62.
- 131 B.-J. Xu, Z.-G. Chi, X.-F. Li, H.-Y. Li, W. Zhou, X.-Q. Zhang, C.-C. Wang, Y. Zhang, S.-W. Liu and J.-R. Xu, *J. Fluoresc.*, 2011, **21**, 433–441.
- 132 Y. Lu, Y. Tan, Y. Gong, H. Li, W. Yuan, Y. Zhang and B. Z. Tang, *Chin. Sci. Bull.*, 2013, **58**, 2719–2722.
- 133 Z.-Q. Liang, Y.-X. Li, J.-X. Yang, Y. Ren and X.-T. Tao, *Tetrahedron Lett.*, 2011, **52**, 1329–1333.
- 134 C. Y. K. Chan, J. W. Y. Lam, Z. Zhao, S. Chen, P. Lu, H. H. Y. Sung, H. S. Kwok, Y. Ma, I. D. Williams and B. Z. Tang, *J. Mater. Chem. C*, 2014, **2**, 4320–4327.
- 135 Y. Liu, Y. Lv, X. Zhang, S. Chen, J. W. Y. Lam, P. Lu, R. T. K. Kwok, H. S. Kwok, X. Tao and B. Z. Tang, *Chem. – Asian J.*, 2012, **7**, 2424–2428.
- 136 J. Zhou, Z. Chang, Y. Jiang, B. He, M. Du, P. Lu, Y. Hong, H. S. Kwok, A. Qin and H. Qiu, *Chem. Commun.*, 2013, **49**, 2491–2493.
- 137 B. Xu, J. He, Y. Dong, F. Chen, W. Yu and W. Tian, *Chem. Commun.*, 2011, **47**, 6602–6604.
- 138 K. Li, W. Qin, D. Ding, N. Tomczak, J. Geng, R. Liu, J. Liu, X. Zhang, H. Liu and B. Liu, *Sci. Rep.*, 2013, **3**, 1150.
- 139 J. Mei, J. Wang, J. Z. Sun, H. Zhao, W. Yuan, C. Deng, S. Chen, H. H. Sung, P. Lu and A. Qin, *Chem. Sci.*, 2012, **3**, 549–558.
- 140 B. Chen, Y. Jiang, L. Chen, H. Nie, B. He, P. Lu, H. H. Y. Sung, I. D. Williams, H. S. Kwok, A. Qin, Z. Zhao and B. Z. Tang, *Chem. – Eur. J.*, 2014, **20**, 1931–1939.
- 141 X. Du and Z. Y. Wang, *Chem. Commun.*, 2011, **47**, 4276–4278.
- 142 B. Yang, X. Niu, Z. Huang, C. Zhao, Y. Liu and C. Ma, *Tetrahedron*, 2013, **69**, 8250–8254.
- 143 C.-A. Chou, R.-H. Chien, C.-T. Lai and J.-L. Hong, *Chem. Phys. Lett.*, 2010, **501**, 80–86.
- 144 J. Li, P. Li, J. Wu, J. Gao, W.-W. Xiong, G. Zhang, Y. Zhao and Q. Zhang, *J. Org. Chem.*, 2014, **79**, 4438–4445.
- 145 S. Chen, Z. Qin, T. Liu, X. Wu, Y. Li, H. Liu, Y. Song and Y. Li, *Phys. Chem. Chem. Phys.*, 2013, **15**, 12660–12666.
- 146 S. Chen, N. Chen, Y. L. Yan, T. Liu, Y. Yu, Y. Li, H. Liu, Y. S. Zhao and Y. Li, *Chem. Commun.*, 2012, **48**, 9011–9013.
- 147 S. J. Ananthakrishnan, E. Varathan, E. Ravindran, N. Somanathan, V. Subramanian, A. B. Mandal, J. D. Sudha and R. Ramakrishnan, *Chem. Commun.*, 2013, **49**, 10742–10744.
- 148 Y. Li, Y. Wu, J. Chang, M. Chen, R. Liu and F. Li, *Chem. Commun.*, 2013, **49**, 11335–11337.
- 149 X. Wang, A. R. Morales, T. Urakami, L. Zhang, M. V. Bondar, M. Komatsu and K. D. Belfield, *Bioconjugate Chem.*, 2011, **22**, 1438–1450.
- 150 C. Gao, G. Gao, J. Lan and J. You, *Chem. Commun.*, 2014, **50**, 5623–5625.
- 151 L. Skardžiūtė, K. Kazlauskas, J. Dodonova, J. Bucevičius, S. Tumkevičius and S. Juršėnas, *Tetrahedron*, 2013, **69**, 9566–9572.
- 152 G.-L. Fu and C.-H. Zhao, *Tetrahedron*, 2013, **69**, 1700–1704.
- 153 B. Wang, Y. Wang, J. Hua, Y. Jiang, J. Huang, S. Qian and H. Tian, *Chem. – Eur. J.*, 2011, **17**, 2647–2655.
- 154 Y. Jiang, Y. Wang, J. Hua, J. Tang, B. Li, S. Qian and H. Tian, *Chem. Commun.*, 2010, **46**, 4689–4691.
- 155 Y. Gao, H. Zhang, T. Jiang, J. Yang, B. Li, Z. Li and J. Hua, *Sci. China: Chem.*, 2013, **56**, 1204–1212.
- 156 W. Huang, H. Wang, L. Sun, B. Li, J. Su and H. Tian, *J. Mater. Chem. C*, 2014, **2**, 6843–6849.
- 157 W. Huang, F. Tang, B. Li, J. Su and H. Tian, *J. Mater. Chem. C*, 2014, **2**, 1141–1148.
- 158 A. Miller, L. Glass-Marmor, M. Abraham, I. Grossman, S. Shapiro and Y. Galboiz, *Clin. Neurol. Neurosurg.*, 2004, **106**, 249–254.
- 159 W. Ling, G. Liew, Y. Li, Y. Hao, H. Pan, H. Wang, B. Ning, H. Xu and X. Huang, *Adv. Mater.*, 2018, **30**, 1800917.
- 160 S. Liu, G. Liang, S. Wang and Q. Hu, *CrystEngComm*, 2025, **27**, 3643–3658.



- 161 H.-Q. Yin, X.-Y. Wang and X.-B. Yin, *J. Am. Chem. Soc.*, 2019, **141**, 15166–15173.
- 162 N. D. Rudd, H. Wang, E. M. A. Fuentes-Fernandez, S. J. Teat, F. Chen, G. Hall, Y. J. Chabal and J. Li, *ACS Appl. Mater. Interfaces*, 2016, **8**, 30294–30303.
- 163 L. Zhang, X. Bi, H. Wang, L. Li and T. You, *Talanta*, 2024, **273**, 125843.
- 164 X. Lin, W. Li, Y. Wen, L. Su and X. Zhang, *Biomaterials*, 2022, **287**, 121603.
- 165 Y. Wang, W. Wu, J. Liu, P. N. Manghnani, F. Hu, D. Ma, C. Teh, B. Wang and B. Liu, *ACS Nano*, 2019, **13**, 6879–6890.
- 166 Y. Wang, W. Wu, D. Mao, C. Teh, B. Wang and B. Liu, *Adv. Funct. Mater.*, 2020, **30**, 2002431.
- 167 F. Hu, D. Mao, Kenry, Y. Wang, W. Wu, D. Zhao, D. Kong and B. Liu, *Adv. Funct. Mater.*, 2018, **28**, 1707519.
- 168 Y. Wang, L. Shi, D. Ma, S. Xu, W. Wu, L. Xu, M. Panahandeh-Fard, X. Zhu, B. Wang and B. Liu, *ACS Nano*, 2020, **14**, 13056–13068.
- 169 D. Mao, F. Hu, Kenry, S. Ji, W. Wu, D. Ding, D. Kong and B. Liu, *Adv. Mater.*, 2018, **30**, 1706831.
- 170 Q. Xu, X. Liao, W. Hu, W. Liu and C. Wang, *J. Mater. Chem. B*, 2021, **9**, 9606–9614.
- 171 E. Barea, C. Montoro and J. A. R. Navarro, *Chem. Soc. Rev.*, 2014, **43**, 5419–5430.
- 172 C. He, J. Cheng, X. Zhang, M. Douthwaite, S. Pattison and Z. Hao, *Chem. Rev.*, 2019, **119**, 4471–4568.
- 173 G. St. Helen, E. Liakoni, N. Nardone, N. Addo, P. Jacob III and N. L. Benowitz, *Cancer Prev. Res.*, 2020, **13**, 153–162.
- 174 C.-Y. Liu, X.-R. Chen, H.-X. Chen, Z. Niu, H. Hirao, P. Braunstein and J.-P. Lang, *J. Am. Chem. Soc.*, 2020, **142**, 6690–6697.
- 175 Y. Zhao, Y. Ye, Z. Wu, J. Jiang, Z. Li, H. Lei, F. Jiang, L. Chen and M. Hong, *Chem. Eng. J.*, 2025, **506**, 159923.
- 176 F. Yang, J. Ma, Q. Zhu, Z. Ma and J. Wang, *ACS Appl. Mater. Interfaces*, 2022, **14**, 22510–22520.
- 177 Y. Wang, B. Yuan, Y.-Y. Xu, X.-G. Wang, B. Ding and X.-J. Zhao, *Chem. – Eur. J.*, 2015, **21**, 2107–2116.
- 178 X. Zhao, Y. Li, Z. Chang, L. Chen and X.-H. Bu, *Dalton Trans.*, 2016, **45**, 14888–14892.
- 179 S. L. Jackson, A. Rananaware, C. Rix, S. V. Bhosale and K. Latham, *Cryst. Growth Des.*, 2016, **16**, 3067–3071.
- 180 H. Peng, Y. Liu, Y. Shen, L. Xu, J. Lu, M. Li, H.-L. Lu and L. Gao, *Molecules*, 2024, **29**, 1657.
- 181 J. Lee, H. Min, Y.-S. Choe, Y. G. Lee, K. Kim, H.-S. Lee and W. Lee, *Sens. Actuators, B*, 2023, **394**, 134359.
- 182 Z. Liu, T. Yang, Y. Dong and X. Wang, *Sensors*, 2018, **18**, 3113.
- 183 H. Onthath, M. R. Maurya, S. Bykkam, H. Morsy, M. Ibrahim, A. E. Ahmed, N.-U. S. S. Riyaz, R. Abuznad, A. Alruwaili, B. Kumar, A. M. Abdullah, P. Kasak and K. K. Sadasivuni, *Macromol. Symp.*, 2021, **400**, 2100202.
- 184 E. Pargoletti, U. H. Hossain, I. Di Bernardo, H. Chen, T. Tran-Phu, J. Lipton-Duffin, G. Cappelletti and A. Tricoli, *Nanoscale*, 2019, **11**, 22932–22945.
- 185 W. Yuan, K. Yang, H. Peng, F. Li and F. Yin, *J. Mater. Chem. A*, 2018, **6**, 18116–18124.
- 186 S. Behi, N. Bohli, J. Casanova-Cháfer, E. Llobet and A. Abdelghani, *Sensors*, 2020, **20**, 3413.
- 187 Y. M. Choi, S.-Y. Cho, D. Jang, H.-J. Koh, J. Choi, C.-H. Kim and H.-T. Jung, *Adv. Funct. Mater.*, 2019, **29**, 1808319.
- 188 B. Cho, K. Lee, S. Pyo and J. Kim, *Micro Nano Syst. Lett.*, 2018, **6**, 1–6.
- 189 M. Fois, T. Cox, N. Ratcliffe and B. de Lacy Costello, *Sens. Actuators, B*, 2021, **330**, 129264.
- 190 J. Park and H. Tabata, *ACS Omega*, 2021, **6**, 21284–21293.
- 191 Y. Zeng, Z. Hua, X. Tian, X. Li, Z. Qiu, C. Zhang, M. Wang and E.-p. Li, *Sens. Actuators, B*, 2018, **273**, 1291–1299.
- 192 Y. Sun, J. Wang, X. Li, H. Du and Q. Huang, *J. Nanopart. Res.*, 2018, **20**, 1–14.
- 193 M. Kumar, A. E. L. Mohajir, F. Berger, M. Raschetti and J.-B. Sanchez, *ACS Appl. Nano Mater.*, 2022, **5**, 9170–9178.
- 194 M. Zhang, Y. Liu, P. Jia, Y. Feng, S. Fu, J. Yang, L. Xiong, F. Su, Y. Wu and Y. Huang, *ACS Appl. Nano Mater.*, 2021, **4**, 1019–1028.
- 195 Y. Wang, Q. Yang, M. Zhao, J. Wu and B. Su, *Anal. Chem.*, 2018, **90**, 10780–10785.
- 196 A. Li, X. Qiao, K. Liu, W. Bai and T. Wang, *Adv. Funct. Mater.*, 2022, **32**, 2202805.
- 197 H.-K. Chang, G. T. Chang, A. K. Thokchom, T. Kim and J. Park, *Sci. Rep.*, 2018, **8**, 5291.
- 198 K. C. To, S. Ben-Jaber and I. P. Parkin, *ACS Nano*, 2020, **14**, 10804–10833.
- 199 A. K. A. Jaini, L. B. Hughes, M. M. Kitimet, K. J. Ulep, M. C. Leopold and C. A. Parish, *ACS Sens.*, 2019, **4**, 389–397.
- 200 B. Zhu, L. Zhu, Y. Wan, S. Deng, C. Zhang and J. Luo, *Sens. Actuators, B*, 2021, **341**, 130011.
- 201 Q.-Y. Li, Z. Ma, W.-Q. Zhang, J.-L. Xu, W. Wei, H. Lu, X. Zhao and X.-J. Wang, *Chem. Commun.*, 2016, **52**, 11284–11287.
- 202 Y. Deng, N. Chen, Q. Li, X. Wu, X. Huang, Z. Lin and Y. Zhao, *Cryst. Growth Des.*, 2017, **17**, 3170–3177.
- 203 Q. L. Guan, F. Xu, Y. Xiao, Z. X. You, F. Y. Bai and Y. H. Xing, *Adv. Mater. Interfaces*, 2022, **9**, 2201547.
- 204 T. Alizadeh and L. Hamedsoltani, *J. Environ. Chem. Eng.*, 2014, **2**, 1514–1526.
- 205 X. Wei, Z. Zhou, T. Hao, H. Li, Y. Zhu, L. Gao and Y. Yan, *RSC Adv.*, 2015, **5**, 44088–44095.
- 206 L. Jiang, H. Liu, M. Li, Y. Xing and X. Ren, *Anal. Methods*, 2016, **8**, 2226–2232.
- 207 R. C. Stringer, S. Gangopadhyay and S. A. Grant, *Anal. Chem.*, 2010, **82**, 4015–4019.
- 208 Y.-f. Hu, Z.-h. Zhang, H.-b. Zhang, L.-j. Luo and S.-z. Yao, *Thin Solid Films*, 2012, **520**, 5314–5321.
- 209 T. Alizadeh, M. R. Ganjali, P. Norouzi, M. Zare and A. Zeraatkar, *Talanta*, 2009, **79**, 1197–1203.
- 210 K. Yan, Y. Yang, Y. Zhu and J. Zhang, *Anal. Chem.*, 2017, **89**, 8599–8603.

- 211 T.-P. Huynh, M. Sosnowska, J. W. Sobczak, C. B. Kc, V. N. Nesterov, F. D'Souza and W. Kutner, *Anal. Chem.*, 2013, **85**, 8361–8368.
- 212 B. Gole, W. Song, M. Lackinger and P. S. Mukherjee, *Chem. – Eur. J.*, 2014, **20**, 13662–13680.
- 213 X. Guo, N. Zhu, S.-P. Wang, G. Li, F.-Q. Bai, Y. Li, Y. Han, B. Zou, X.-B. Chen, Z. Shi and S. Feng, *Angew. Chem., Int. Ed.*, 2020, **59**, 19716–19721.
- 214 Y. Cai, H. Zhu, W. Zhou, Z. Qiu, C. Chen, A. Qileng, K. Li and Y. Liu, *Anal. Chem.*, 2021, **93**, 7275–7282.
- 215 Y. Zhang, T. Xiong, A. F. Möslin, S. Mollick, V. Kachwal, A. S. Babal, N. Amin and J.-C. Tan, *Appl. Mater. Today*, 2022, **27**, 101434.
- 216 X.-F. Wang, G.-X. Liu, X. D. Zhang, L. Luo and K. Chen, *J. Mater. Chem. C*, 2025, 15091–15098.
- 217 C. Wang, T. Zhang, L.-X. Sun, Y.-H. Xing and F.-Y. Bai, *Inorg. Chem. Front.*, 2023, **10**, 7351–7358.
- 218 R. Wang, H. Qi, H. Zheng and Q. Jia, *Chin. Chem. Lett.*, 2024, **35**, 109215.